Atmospheric Environment 202 (2019) 190–211

Contents lists available at ScienceDirect

Atmospheric Environment

journal homepage: www.elsevier.com/locate/atmosenv

Evaluation of night-time aerosols measurements and lunar irradiance models in the frame of the first multi-instrument nocturnal intercomparison campaign

A. Barreto[a,b,c], R. Román[c,d,e], E. Cuevas[b,*], D. Pérez-Ramírez[d,e], A.J. Berjón[c,b], N. Kouremeti[f], S. Kazadzis[f], J. Gröbner[f], M. Mazzola[g], C. Toledano[c], J.A. Benavent-Oltra[d,e], L. Doppler[h], J. Juryšek[i], A.F. Almansa[a,b,c], S. Victori[a], F. Maupin[a], C. Guirado-Fuentes[c,b], R. González[c], V. Vitale[g], P. Goloub[j], L. Blarel[j], L. Alados-Arboledas[d,e], E. Woolliams[k], S. Taylor[k], J.C. Antuña[c], M. Yela[l]

[a] Cimel Electronique, Paris, France
[b] Izaña Atmospheric Research Center, Meteorological State Agency of Spain (AEMET), Spain
[c] Grupo de Óptica Atmosférica, Universidad de Valladolid, Valladolid, Spain
[d] Department of Applied Physics, University of Granada, Granada, Spain
[e] Andalusian Institute for Earth System Research, IISTA-CEAMA, University of Granada, Junta de Andalucía, Granada, Spain
[f] Physikalisch-Meteorologisches Observatorium Davos and World Radiation Center (PMOD/WRC), Davos, Switzerland
[g] National Research Council, Institute of Atmospheric Sciences and Climate (CNR-ISAC), Bologna, Italy
[h] Deutscher Wetterdienst, Meteorologisches Observatorium Lindenberg – Richard Assmann Observatorium (DWD, MOL-RAO), Lindenberg, Germany
[i] Czech Academy of Sciences, Prague, Czech Republic
[j] Laboratoire d'Optique Amosphérique (LOA), Universitée des Sciences et Technologies de Lille, Villeneuve d'Ascq, France
[k] National Physical Laboratory (NPL), London, United Kingdom
[l] Instrumentation and Atmospheric Research Department, National Institute for Aerospace Technology (INTA), Madrid, Spain

ARTICLE INFO

Keywords:
Lunar photometry
Star photometry
AOD
ROLO

ABSTRACT

The first multi-instrument nocturnal aerosol optical depth (AOD) intercomparison campaign was held at the high-mountain Izaña Observatory (Tenerife, Spain) in June 2017, involving 2-min synchronous measurements from two different types of lunar photometers (Cimel CE318-T and Moon Precision Filter Radiometer, LunarPFR) and one stellar photometer. The Robotic Lunar Observatory (ROLO) model developed by the U.S. Geological Survey (USGS) was compared with the open-access ROLO Implementation for Moon photometry Observation (RIMO) model. Results showed rather small differences at Izaña over a 2-month time period covering June and July, 2017 (±0.01 in terms of AOD calculated by means of a day/night/day coherence test analysis and ± 2% in terms of lunar irradiance). The RIMO model has been used in this field campaign to retrieve AOD from lunar photometric measurements.

No evidence of significant differences with the Moon's phase angle was found when comparing raw signals of the six Cimel photometers involved in this field campaign.

The raw signal comparison of the participating lunar photometers (Cimel and LunarPFR) performed at co-incident wavelengths showed consistent measurements and AOD differences within their combined uncertainties at 870 nm and 675 nm. Slightly larger AOD deviations were observed at 500 nm, pointing to some unexpected instrumental variations during the measurement period.

Lunar irradiances retrieved using RIMO for phase angles varying between 0° and 75° (full Moon to near quarter Moon) were compared to the irradiance variations retrieved by Cimel and LunarPFR photometers. Our results showed a relative agreement within ± 3.5% between the RIMO model and the photometer-based lunar irradiances.

The AOD retrieved by performing a Langley-plot calibration each night showed a remarkable agreement (better than 0.01) between the lunar photometers. However, when applying the Lunar-Langley calibration using RIMO, AOD differences of up to 0.015 (0.040 for 500 nm) were found, with differences increasing with the

* Corresponding author.
E-mail address: ecuevasa@aemet.es (E. Cuevas).

https://doi.org/10.1016/j.atmosenv.2019.01.006
Received 27 June 2018; Received in revised form 29 December 2018; Accepted 6 January 2019
Available online 19 January 2019

Moon's phase angle. These differences are thought to be partly due to the uncertainties in the irradiance models, as well as instrumental deficiencies yet to be fully understood.

High AOD variability in stellar measurements was detected during the campaign. Nevertheless, the observed AOD differences in the Cimel/stellar comparison were within the expected combined uncertainties of these two photometric techniques. Our results indicate that lunar photometry is a more reliable technique, especially for low aerosol loading conditions.

The uncertainty analysis performed in this paper shows that the combined standard AOD uncertainty in lunar photometry is dependent on the calibration technique (up to 0.014 for Langley-plot with illumination-based correction, 0.012–0.022 for Lunar-Langley calibration, and up to 0.1 for the Sun-Moon Gain Factor method). This analysis also corroborates that the uncertainty of the lunar irradiance model used for AOD calculation is within the 5–10% expected range.

This campaign has allowed us to quantify the important technical difficulties that still exist when routinely monitoring aerosol optical properties at night-time. The small AOD differences observed between the three types of photometers involved in the campaign are only detectable under pristine sky conditions such as those found in this field campaign. Longer campaigns are necessary to understand the observed discrepancies between instruments as well as to provide more conclusive results about the uncertainty involved in the lunar irradiance models.

1. Introduction

In the past decades, sunlight photometric measurements have been used to provide reliable information about optical, micro-physical and radiative aerosol properties. This valuable information has been used to compile long-term and global Aerosol Optical Depth (AOD) records and other aerosol properties in order to better understand their role in the Earth's climate. The contribution of the current sun photometer networks is also important for aerosol transport models, either by assimilation or in validation studies (Cesnulyte et al., 2014; Cuevas et al., 2015), in validation of satellite products (Zhang and Reid, 2010; Tanré et al., 2011; Sayer et al., 2013; Li et al., 2016), or as additional information to improve aerosol products from lidar systems (Lopatin et al., 2013; Chaikovsky et al., 2016; Benavent-Oltra et al., 2017). Nevertheless, AOD data provided by sun photometers is severely restricted since it is limited to daytime, making full diurnal (24 h) aerosol monitoring and characterization impossible. This seriously constrains the study of atmospheric processes in which day-to-night variations play an important role. For example, solar radiation favours aerosol nucleation in the daytime (Jokinen et al., 2017); atmospheric dynamics is affected by convective processes in the daytime; and local and anthropogenic aerosol sources as traffic, domestic heating or agricultural straw open burning usually follow a well-defined time pattern. As a consequence, the exclusive use of daytime observations might introduce a bias in climatological studies. This limitation is critical in high latitude and polar regions.

Since the first and pioneering attempts to estimate AOD at night developed by Leiterer et al. (1995); Esposito et al. (1998); Herber et al. (2002) and Berkoff et al. (2011), the need to monitor aerosols in a routine way in the absence of solar radiation has led to remarkable efforts in the scientific community, especially by polar atmospheric researchers. A number of studies have been focused on aerosol monitoring in the Arctic, with the works developed by Tomasi et al. (2007, 2012); Mazzola et al. (2012); Tomasi et al. (2015) and Stone et al. (2010) as the most notable examples. Mazzola et al. (2012) evaluated the capabilities of sun photometers to retrieve AOD in such a harsh environment through two intercomparison campaigns, held in Ny-Ålesund (Norway) and Izaña (Spain) in 2006 and 2008, respectively. This study confirmed sun photometry to be a valid technique in polar and high latitude pristine conditions.

There are currently only a few techniques capable of estimating AOD at night-time: 1. Ground-based or space-borne lidars, 2. Stellar photometry and 3. Lunar photometry. In-situ vertical integrated aerosol extinction measurements from aircraft or balloons are also plausible procedures to estimate AOD at day and night-time. However, these techniques are generally quite limited because of the effort and costs associated with these types of operations.

Lidar systems permit determining vertical profiles of aerosol optical and micro-physical properties. Nevertheless, lidar retrievals usually require some physical or mathematical constraints in inversion algorithms to allow the quantitative interpretation of the lidar backscatter signal (Fernald, 1984; Klett, 1985). These assumptions usually require passive AOD information, and therefore demonstrate the necessity of the synergy between lidar and photometers (Cuesta et al., 2008; Lopatin et al., 2013; Chaikovsky et al., 2016; Benavent-Oltra et al., 2017) both for day and night period.

Early studies have proven the stellar photometry to be a plausible technique for aerosol monitoring at night-time (Leiterer et al., 1995; Pérez-Ramírez et al., 2012a, 2015; Baibakov et al., 2015). It is considered the de facto reference for all AOD nocturnal measurements (O'Neill et al., 2016), with an expected standard uncertainty in AOD measurements estimated in 0.02–0.03 (Baibakov et al., 2015). However, its complexity, expensive infrastructure and logistics, and automation constraints, still represent an important limitation for the operational use of star measurements, especially in establishing a global operational network.

Lunar photometry is another approach to extend remote sensing capabilities during nocturnal period. Photometric stability of the lunar surface allows the Moon to be used as a well-defined target. The Moon is considered photometrically stable at a level of 10^{-8} per year (Kieffer, 1997). However, despite its long-term stability, important drawbacks in moon photometry still exist with the most important one being related to the variability of the reflected solar irradiance with the Moon's cycle. As a consequence, a precise exo-atmospheric lunar irradiance model is mandatory in moon photometry (Berkoff et al., 2011; Barreto et al., 2013, 2016). The uncertainty in AOD retrieved using this technique is therefore dependent on the uncertainty of the lunar irradiance model itself. The United States Geological Survey (USGS) Robotic Lunar Observatory (ROLO) model, developed by Kieffer and Stone (2005) is considered the most reliable lunar radiometric reference available until now, with an estimated Type A standard uncertainty of 1% in the lunar reflectance (Kieffer and Stone, 2005) and an expected Type B standard uncertainty in the Moon's irradiance ranging from 5% to 10% (Stone and Kieffer, 2004). Barreto et al. (2016) observed a phase angle dependence on the AOD differences (CE318-T nocturnal measurements compared to reference daytime data) performed at the high-mountain Izaña Observatory, with systematic errors in the ROLO model or instrumental problems in the CE318-T photometer as the most probable causes for such dependence. Other authors also found important variations between on-orbit lunar irradiances and the irradiances predicted by the USGS/ROLO model (Viticchié et al., 2013; Lacherade et al., 2013, 2014).

Accurate AOD measurements at night from either moon or star photometry are difficult to obtain due to the low incoming signals:

between 5 and 6 orders of magnitude lower than the Sun's irradiance in the case of the Moon between the first and last quarters, and more than 4 orders of magnitude lower in the case of Sirius, the brightest star in the night sky (Berkoff et al., 2011). Consequently, there are significant limitations in the sensors which can be used to monitor aerosols at night. The increase in the dynamic range and sensitivity of these sensors as well as the improvement of the electronics required to increase the signal-to-noise ratio (SNR) remain a challenging subject of ongoing interest. There are currently only a few instruments with capability of monitoring AOD at night: the CE318-T (Barreto et al., 2016), developed by Cimel Electronique, the Moon Precision Filter Radiometer, LunarPFR (Kouremeti et al., 2016), developed by the Physical Meteorological Observatory in Davos (PMOD) which serves as the World Radiation Center (WRC), and the only five stellar photometers existing at present plenty devoted to routine aerosol monitoring. Four of these stellar photometers were developed by Dr. Schulz and Partner GmbH, and are located in Ny-Ålesund (Norway), Eureka and Sherbrooke (Canada) and Lindenberg (Germany). The fifth one is the EXCALIBUR star photometer (EXtinction CAmera and LumIiance BackgroUnd Register), developed by Astronómica S.L., belonging to the Atmospheric Physics Group of the University of Granada (UGR), installed in Granada, Spain (Pérez-Ramírez et al., 2008a, 2012a).

It is of critical importance to identify standard procedures to retrieve aerosol properties at night as well as to recognize and correct possible instrumental problems. In this sense, it is important to rule out potential instrumental problems as the cause of the phase angle dependence on AOD uncertainty found in previous studies (Barreto et al., 2016, 2017; Juryšek and Prouza, 2017). The only way to achieve this goal is by means of intercomparison campaigns involving the different available instruments with nocturnal remote sensing capabilities. Until now, only a short nocturnal AOD intercomparison campaign has been undertaken, involving four nights of collocated measurements from a lunar photometer CE318-T and a stellar photometer in Granada (Barreto et al., 2016). It is also important to assess the uncertainty of the USGS/ROLO model, and to compare its outputs with self-implemented models developed by other scientific groups. One of the main objectives of the scientific community nowadays is to have an unique reference model for lunar irradiance or to reconcile the existing ones. There are various current and ongoing projects aimed at providing an improved ROLO model or a completely new and improved lunar irradiance model in the near future.

In this paper we address the main problems currently encountered in night-time photometry. Firstly, we present a description of the different instruments involved in this field campaign, we describe the process of cloud screening and quality control as well as an overview of the common methods used for calibration in lunar photometry. Secondly, a self-implemented lunar irradiance model based on the USGS/ROLO model (ROLO Implementation for Moon photometry Observation, RIMO) is also presented. RIMO is an open-access development performed under the initiative of several research teams with the participation of the Polar-AOD group, which started with this challenging issue a decade ago in the frame of the International Polar Year 2007–08 (Tomasi et al., 2012). RIMO is intended to serve as a freely-available model until a new and improved lunar irradiance model is available to the scientific community. Finally, we present the first comparison of coincident night-time photometric measurements from different lunar photometers (six CE318-T instruments and a LunarPFR) and a stellar photometer (EXCALIBUR photometer). The performance of the existing nocturnal instrumentation were evaluated in terms of both raw signals and AOD.

2. Night-time photometry field campaign

2.1. Aim of the field campaign

This campaign has been jointly organized by the Izaña Atmospheric Research Center (IARC, belonging to the State Meteorological Agency of Spain, AEMET) and the University of Valladolid (UVa), with a parallel workshop on lunar photometry taking place at the time of this campaign. The main objectives for this workshop were to evaluate the instruments' performance under pristine sky conditions, promote dialogue and exchange of experience among researchers, work on the development of the new RIMO model, and develop collaborations not only between researchers but also with the instrument manufacturers to strengthen Polar-AOD activities. Nocturnal photometric measurements were carried out between 1 June 2017 and 17 June 2017 (15 nights with Moon between first to last quarter). The site was selected to ensure measurements were carried out in pristine conditions with June chosen in order to minimize the impact of possible Saharan dust intrusions over the Observatory.

2.2. Test site

This first nocturnal multi-instrumental comparison campaign has been held at the Izaña Observatory (http://izana.aemet.es), a high-mountain Global Atmospheric Watch (GAW) station located at 2400 m a.s.l. in Tenerife, Canary Islands, Spain (28.31°N, 16.49°W). This Observatory is managed by IARC-AEMET, and is a World Meteorological Organization (WMO) Commission for Instruments and Methods of Observations (CIMO) Testbed for Aerosols and Water Vapour Remote Sensing Instruments. It is precisely this Testbed infrastructure that has allowed us to undertake the field campaign and the parallel workshop. A detailed information of the Izaña Observatory facilities and its activities can be found in Cuevas et al. (2017).

2.3. Instruments

We present in Table 1 a brief description of the different photometers involved in the field campaign: six Cimels CE318-T, a LunarPFR and a stellar photometer.

It is important to emphasize that the filter responses of the three different instruments differ in central wavelength by 24–27 nm, ~

Table 1
Details of the instruments involved in the field campaign, including central wavelength, Field of view (FOV), full width at half maximum (FWHM) in the visible (VIS), ultraviolet (UV) and near infrared (NIR) spectral bands, and measurement period.

Instrument type	Number	Institution	Central Wavelength (nm)	FOV	FWHM	Meas. period
Cimel	#971	IARC	340.6, 379.9, 439.5, 500.6, 674.8, 870.4, 936.7, 1019.3, 1640.5	1.26°	2 nm (UV), 10 nm (VIS), 40 nm (NIR)	2–17 June
	#915	Lille	340.6, 379.9, 439.5, 500.6, 674.8, 870.4, 936.7, 1019.3, 1640.5	1.26°	2 nm (UV), 10 nm (VIS), 40 nm (NIR)	2–17 June
	#919	MOL-RAO	340.6, 379.3, 440.1, 500.4, 674.8, 868.9, 937.5, 1019.8, 1640.2	1.26°	2 nm (UV), 10 nm (VIS), 40 nm (NIR)	2–17 June
	#942	UVa	340.6, 379.9, 439.5, 500.6, 674.8, 870.4, 936.7, 1019.3, 1640.5	1.26°	2 nm (UV), 10 nm (VIS), 40 nm (NIR)	5–17 June
	#945	Lille	340.6, 379.9, 439.5, 500.6, 674.8, 870.4, 936.7, 1019.3, 1640.5	1.26°	2 nm (UV), 10 nm (VIS), 40 nm (NIR)	2–17 June
	#949	UVa	340.6, 379.9, 439.5, 500.6, 674.8, 870.4, 936.7, 1019.3, 1640.5	1.26°	2 nm (UV), 10 nm (VIS), 40 nm (NIR)	2–17 June
LunarPFR	–	PMOD-WRC	412.4, 501.2, 675.6, 861.3	1.30°	5 nm (4 nm for 412.4 nm)	8–17 June
Star (EXCALIBUR)	–	UGR	379.1, 436.8, 500.7, 532.0, 670.0, 879.5, 1020.0	–	10 nm (3 nm for 532.0 nm)	2–9 June

9 nm, < 5 nm and < 1 nm in the 440 nm, 870 nm, 675 nm and 500 nm spectral bands, respectively. This analysis compares raw signals and AOD at similar wavelengths. In this sense, the comparison involving LunarPFR measurements has been constrained to the Cimel and stellar spectral bands with differences in central wavelengths of up to 9 nm. This constraint limits the comparison to three spectral bands (500, 675 and 870 nm). A similar threshold in the central wavelength difference was used in McArthur et al. (2003) in the visible portion of the spectrum. As these authors claimed, AOD is not expected to vary significantly as a result of a 9 nm difference central-wavelength shift in this spectral range (Cuevas et al., 2018), although high ozone absorption under low AOD conditions might introduce unwanted AOD variations in the comparison analysis. This effect has been discarded in this study taking into account that the central-wavelength shift in those spectral bands with important ozone absorption is < 0.8 nm for Cimel and lunarPFR, and < 4.8 nm for Cimel and stellar. Cimel and stellar measurements have been compared at four coincident spectral bands: 440, 500, 675 and 870 nm.

Full Width at Half Maximum (FWHM) bandwidths of the three different instruments are within the typical range of narrow field-of-view photometers (5–10 nm).

Synchronous Cimel, LunarPFR and stellar measurements are used in this comparison analysis within a 2-min time window. The synchronization between instruments has been ensured automatically by means of frequent adjustments using reference time from an internal web server. Cimel and LunarPFR checked the time reference automatically three times per day while the stellar synchronized its measurements once per day, at the beginning of its operation. The measurements synchronization has been double checked manually by the staff involved in the continuous operation of the instruments during the field campaign.

2.3.1. Cimel CE318-T

The sun-sky-lunar (Triple) Cimel CE318-T is a photometer developed by Cimel Electronique (Barreto et al., 2016), capable of making both day and night-time photometric measurements. CE318-T, hereinafter referred to as Cimel, performs both direct sun and sky radiance observations during the daytime, providing detailed aerosol properties (Nakajima et al., 1996; Dubovik et al., 2006; Torres et al., 2017), but only direct moon measurements at night-time. Despite the lack of radiance measurements at night, there are some studies in the literature aimed at providing information on the properties of aerosols at night (O'Neill et al., 2016; Torres et al., 2017; Román et al., 2017).

The Cimel photometer is composed of an optical head, a control unit and a robot for sun/moon tracking. CE318-T provides additional and enhanced features compared with the former standard CE318-N sun photometer currently used in the Aerosol Robotic Network (AERONET) (Holben et al., 1998). The CE318-T photometer includes a new tracking system with micro-stepping technology to control the robot, and a new four-quadrant sensor with higher sensitivity for solar and lunar measurements. This new photometer incorporates in the control unit a software to calculate the position of the Sun and the Moon. For every measurement, the robot executes an automatic pointing which directs the sensor head to the Sun/Moon with a pointing resolution of 0.003° on both axes. After that, the four-quadrant detector is used to improve the tracking before each measurement sequence, pointing to the center of the illuminated part of the Moon.

Cimel measurements are performed at eight nominal wavelengths (340, 380, 440, 500, 675, 870, 940 and 1020 nm) using a silicon photodiode detector plus two additional measurements at 1020 nm and 1640 nm using an InGaAs detector. It has an approximate field of view (FOV) of 1.29° and about 10 nm FWHM bandwidth in visible spectral bands. Information from UV spectral bands is only used in the daytime, due to the low signal in this spectral range at night. The Cimel makes a sequence of three consecutive measurements at each wavelength 30 s apart, called triplets. Triplets measurement allows us to detect and remove data contaminated by clouds, through the normalized range (NR) between these three measurements (defined as the difference between maximum and minimum divided by the mean). The method used in this work for cloud-screening at night-time will be presented in Sect. 3.1.4. The Cimel also routinely performs dark current estimation through a sequence of eight measurements with the two detectors obstructed before each direct moon observation. The average value of dark current has been directly subtracted from the direct moon signal measured by the Cimel.

The non-linearity of the Cimel has been evaluated at the National Physical Laboratory (NPL) using the double-aperture method (Theocharous et al., 2004). This evaluation found the instrument to be highly linear, with an average non-linear factor of 0.03%. A non-linearity factor of 0% means a perfect linearity.

Instrument stability of the CE318-T photometer was estimated by Barreto et al. (2016) in 0.1–0.5% (1% for 440 nm), including atmospheric variability during the measurement as well as pointing uncertainties. All these values correspond to Type A uncertainties ($k = 1$).

A total of six different CE318-T photometers, all part of AERONET, participated in this field campaign, which belong to Izaña Observatory (IARC: #971), Lindenberg Meteorological Observatory – Richard Assmann Observatory (MOL-RAO: #919), University of Valladolid (UVa: #942 and #949) and University of Lille (Lille: #915 and #945). The characteristics of each one are described in Table 1. The six instruments execute the same measurement protocol in the daytime, in which direct sun measurements (triplets) are made at 3-min intervals as long as sky observations are not performed (almucantar and principal plane measurements). Regarding the measurement protocol at night-time, direct moon measurements are made every three minutes, with the exception of UVa instruments (#942 and #949), which measure every five minutes.

In this work, IARC #971 is referred to be the master in the intercomparison campaign. This instrument has been detected to be stable and reliable, and therefore, it serves as a reference instrument to calibrate secondaries or field instruments.

2.3.2. LunarPFR

The LunarPFR is a standard PFR photometer that has been developed at PMOD/WRC based on the sun-PFR experience. Compared to the sun-PFR, the LunarPFR has enhanced sensitivity in its four different optical channels. Every channel has a band-pass filter with nominal wavelength at 412, 500, 675 and 862 nm. As for the sun-PFR, the sensor is stabilized at 20 °C. The LunarPFR filter functions, measured with the PMOD/WRC ATLAS tunable laser, have a bandwidth (FWHM) of 4 nm for 412 nm and 5 nm for the rest of the spectral bands, and a plateau (90%) of 2 nm and 3 nm, respectively. The data acquisition (DAQ) system (OWEL/PMOD) perform measurements from −5 V to +10 V with a 22 bits A/D converter. The LunarPFR is mounted on a Kipp & Zonen Soly2 tracker. This tracker is operated in manual mode since both the tracker sun-sensor and the PFR-four quadrant sensor are insensitive to lunar irradiance, pointing to the center of the lunar disk. The instrument is optically aligned to the Moon and the stability/efficiency of the tracking relies on the mechanical stability of the setup with respect to the FOV homogeneity tolerances. The estimated uncertainty of the tracking positioning, by testing the passive tracking during the day, is 0.1° (coverage factor $k = 1$).

The four photodiode sensors of the LunarPFR are placed in a square arrangement. The FOV of each one of the LunarPFR channels is 1.3°, defined by the front (mask) and the sensor apparatus. The LunarPFR FOVs have a plateau of 1°, with a homogeneity uncertainty of ± 0.3% ($k = 1$). However, the center of the 862 nm and 500 nm channels plateau have an offset of −0.1° and 0.2° with respect to 675 nm and 412 nm channels, respectively. These offsets increase the homogeneity uncertainty to ± 0.85% ($k = 1$) for 500 nm while the rest of the wavelengths remain unaffected. This feature, depending on the tracking stability, might affect both the Langley calibration and the AOD

retrievals, increasing the expected uncertainty in AOD due to the FOV in-homogeneities from 0.003 to 0.020 ($k = 1$) for the 500 nm spectral band.

The linearity of the DAQ system has been checked with the PMOD/WRC data logger calibration unit, finding a non-linearity factor better than 0.15% (0.05% for the dark corrected signals).

With this information, uncertainties associated to non-linearity and pointing errors are estimated to be 0.05% and 0.3–0.85%, respectively. The instrument's stability has been estimated by means of the combination of the standard deviation of voltages (0.1%) and the standard deviation of dark measurements (0.1%). All these values correspond to Type A uncertainties ($k = 1$).

The measurement sequence of the LunarPFR during the campaign is 10 lunar measurements with an integration time of 3 s each followed by five similar dark count measurements.

The LunarPFR has been developed within the Svalbard Science Forum funded project with the initiative of Institute of Atmospheric Sciences and Climate (ISAC). This instrument has been performing measurements since 2014 in Ny-Ålesund (Norway) during the polar winter in collaboration with ISAC and the Norwegian Institute for Air Research (NILU), aiming to provide a continuous AOD series for satellite validation purposes.

2.3.3. Stellar photometer

The EXCALIBUR (EXtinction CAmera and LumInance BackgroUnd Register, Astronomica S.L.) stellar photometer measures direct star irradiance using a 30 cm telescope (Schmidt-Cassegrain optical design) and a CCD camera (SBIG ST8-XME) as detector. Measurements are made for stars that are isolated and whose emission is considered stable with time. Spectral measurements are possible through interference filters centered at 380, 440, 500, 532, 670, 880 and 1020 nm, which allow direct estimation of AODs. All filters have a FWHM of approximately 10 nm, similar to the Cimel spectral bands, with the only exception of the spectral band centered at 532 nm, with a FWHM of 3 nm. The EXCALIBUR measurement time varies with the interference filters and the type of star measured. For 670 nm and 500 nm measurement times are usually below 1 s while for 380 nm and 1020 nm measurement times are between 15 s and 100 s. The rest of filters present intermediate measurement times. An external CCD camera, attached and perfectly aligned with the telescope, is used to guarantee adequate alignment for a given star. More details of this instrument design can be found in Pérez-Ramárez et al. (2008a). Source of errors in EXCALIBUR measurements have been studied in detail in Pérez-Ramárez et al. (2008b). Measurements are done within the linearity zone of the camera, between 1500 and 45000 counts. The CCD camera is cooled at −20 °C throughout its operation, minimizing the effects of bias with temperature. Dark current is also correctly estimated for each exposure time. The effects of shutter are also considered, which is particularly important for exposure times below 0.3 s. Finally, the effects of non-homogeneity between pixels is corrected by means of flat fields performed during the afternoon before starting EXCALIBUR night-time operations.

The star photometer EXCALIBUR is calibrated using the Astronomical Langley method for each selected star (Pérez-Ramárez et al., 2011). The effects of atmospheric turbulence are also considered because it is an additional source of errors due to the low signal-to-noise ratio. This yields to uncertainties in measured AODs of 0.02 for $\lambda <$ 800 nm and 0.01 for $\lambda >$ 800 nm. The instrument follows strict procedures for cloud screening and data quality control (Pérez-Ramárez et al., 2012b). Details of calibration and data quality control for EXCALIBUR are given in Section 3.2. We note that stellar photometry is a technique that does not depend on any lunar irradiance models and therefore it will serve as an independent validation for AODs retrieved by means of lunar photometry.

2.3.4. Micro-Pulse Lidar (MPL-3) backscatter profiles

Information extracted from the MPL-3 (Spinhirne et al., 1995) has been used as ancillary information for assessing the stability in AOD conditions during this field campaign. This instrument operates full time at Santa Cruz de Tenerife station (28.5°N, 16.2°W; 52 m a.s.l.) within the NASA/MPLNET network (http://mplnet.gsfc.nasa.gov) providing backscattered signal at 523 nm in 1-min integrated time period and at 75 m vertical resolution. This instrument is jointly managed by the National Institute for Aerospace Technology (INTA) and the IARC. Further details of this system can be found at Campbell et al. (2002).

2.4. Aerosol content and Moon's illumination during the field campaign

The evolution of the Moon's phase angle (g) over this measurement period is shown in Fig. 1. This magnitude ranged from −84.7° to 74.6°, which corresponds to a Moon's illumination factor (IF) ranging from 54.6% to 63.2%.

The evolution of the lidar range corrected signal at 523 nm during the field campaign is shown in Fig. 2. Some high clouds were observed from 5 June to 7 June, as well as on 11 June. A dust intrusion was also observed from 10 June to 12 June, below Izaña's level. This figure demonstrates the low, stable aerosol conditions at the Observatory during the field campaign.

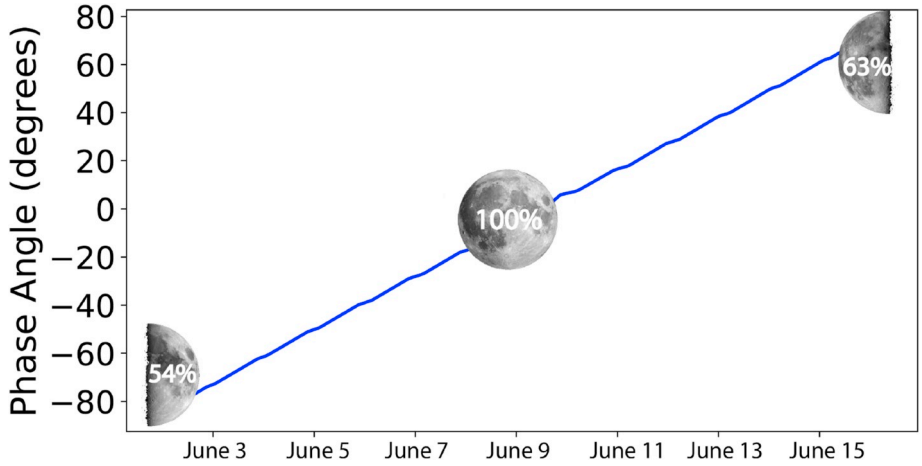

Fig. 1. Phase angle evolution (in degrees) during the measurement period in the nocturnal field campaign.

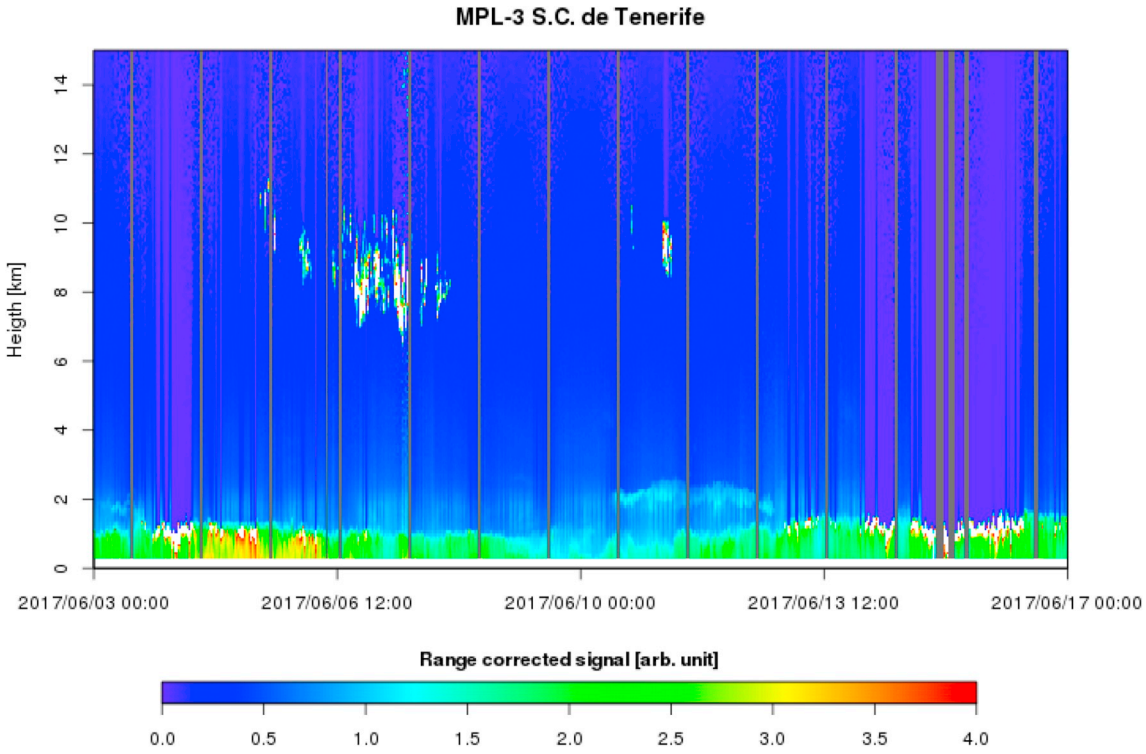

Fig. 2. Micro-Pulse Lidar (MPL-3) range corrected signals at 523 nm obtained at Santa Cruz de Tenerife station (60 m a.s.l.). Grey vertical lines represent the absence of measurements due to rain or direct solar incidence in the detector at noon.

3. Methodology and supporting information

3.1. Lunar photometry calibration and cloud-screening

3.1.1. Classic Langley calibration method applied to lunar observations (Langley-plot calibration)

The most utilized procedure for calibrating sun photometers involves the estimation of the voltage measured by the instrument at the top of the atmosphere by extrapolation of the voltage curve to zero air mass (Shaw, 1979; Shaw, 1983). This calibration procedure, known as the Langley-plot method, is an application of the Beer–Lambert–Bouguer Law. It has been proposed as the standard calibration method by WMO although its application is restricted to stable and preferably low AOD conditions, usually found only at high altitudes. Eq. (1) gives the fundamental equation of this technique.

$$ln(V_j) = ln(V_{0,j}) - m(\theta)\cdot\tau_j \quad (1)$$

In this equation, V_j is the instrument's voltage measured in the j^{th} spectral band, $V_{0,j}$ is the instrument's calibration constant, m represents the optical air mass (dependent on the Moon's zenith angle, θ), and τ_j is the total optical depth (including both atmospheric attenuators and aerosols). In this paper, optical air mass was calculated according to Kasten and Young (1989). AOD can be obtained by means of the following equation:

$$AOD_j = \frac{ln(V_{0,j}) - ln(V_j) - m_{atm}(\theta)\cdot\tau_{atm,j}}{m_a(\theta)} \quad (2)$$

where m_{atm} represents the optical air mass for molecular atmospheric attenuators; m_a that for aerosols, both of which depend on the Moon's zenith angle (θ); and τ_{atm} is the optical depth of each atmospheric attenuator with the exception of aerosols.

This conventional calibration technique has to be modified to allow the Moon to be used as the light source for calibration. In contrast to the Sun, the Moon's irradiance changes continuously over the lunar cycle and even over the ~ 2 h time period of the Langley calibration. The phase angle variation during this period has been found to vary between 0.4% near the full Moon and 0.6% near the quarters. Overall, the Langley-plot calibration technique can be considered to be a robust calibration technique to be applied at night-time, because it is only valid in the course of one specific night (calibration and instrumental problems are strongly minimized). However, the relative variation of the Moon's illumination during the Langley calibration is an important problem to overcome.

An illumination-based correction procedure has been developed in this work to correct the Moon's illumination change over the Langley period, accounting for the variation of lunar irradiance over this short period. Taking the Langley calculation at the half point as a reference, we propose a correction factor applied on the instrument's signal:

$$RI_0 = \frac{I_{0,j}^{ref}}{I_{0,j}} \quad (3)$$

and therefore the Langley equation with the illumination-based correction is:

$$ln[V_j\cdot RI_0] = ln(V_{0,j}^c) - m(\theta)\cdot\tau_j \quad (4)$$

This correction factor, RI_0, corrects for the lunar irradiance change during the Langley calibration. It is a ratio between the lunar irradiance at the half mark of the Langley ($I_{0,j}^{ref}$) and the lunar irradiance at the time t_j in the calibration period ($I_{0,j}$). This ratio is obtained from a lunar irradiance model that corrects for lunar phase and libration changes.

As a result, any uncertainty associated with the lunar irradiance model has only minimum impact on the determined AOD. The Langley calibration method is also insensitive to a systematic instrument bias, as long as it is constant throughout the night. However, the calibration method can only be applied under stringent atmospheric conditions (pristine skies), which should be met every night. The difficulty of finding exceptionally clear, clean nights in most stations makes this method of calibration only applicable in very specially chosen locations (high altitude, clear skies).

The combined standard uncertainty estimation of the AOD retrieved

by means of a Langley-plot calibrated instrument, including this new illumination-based correction procedure, is summarized in Eq. (6), where V^c is defined as follows:

$$V^c = V \cdot RI_0 \tag{5}$$

$$u_{AOD^2} = \frac{1}{m^2}\left(\frac{u^2(V_0^c)}{(V_0^c)^2} + \frac{u^2(V^c)}{(V^c)^2}\right) = \frac{1}{m^2}\left(\frac{u^2(V_0^c)}{(V_0^c)^2} + \frac{u^2(V)}{(V)^2} + \frac{u^2(RI_0)}{(RI_0)^2}\right) \tag{6}$$

This uncertainty is modulated by the air mass term, and therefore maximum AOD errors are expected for $m = 1$ (the Moon in the meridian passage). The instrumental uncertainty ($u(V)$) can be expressed as a contribution of non-linearity ($u(V_{lin})$) and stability in measurement ($u(V_{stab})$) errors ($u(V_{stab})$ in Eq. (7)).

$$u_V^2 = \frac{u^2(V_{lin})}{V^2} + \frac{u^2(V_{stab})}{V^2} \tag{7}$$

Values for $u(V_{lin})$ and $u(V_{stab})$ are given in Sections 2.3.1 and 2.3.2 for Cimel and LunarPFR, respectively. With this information, the instrument combined standard uncertainty ($k = 1$) for Cimel has been estimated to be 0.1–0.5% (1.0% in 440 nm), and 0.33–0.86% for LunarPFR.

The uncertainty ($k = 1$) associated with the RI_0 term ($u(RI_0)$) has been estimated from the maximum percentage of variation in the Moon's phase angle during one night (0.6%). The uncertainty associated with the Langley intercept, the top-of-atmosphere signal ($u(V_0^c)$), has been estimated by means of a Type A uncertainty evaluation. Two components have been identified to contribute to $u(V_0^c)$. First, we consider the uncertainty associated with the intercept as determined from the linear least squares fitting routine (0.2–0.5%). Another contribution comes from the extent to which the data is consistent with the straight line model. This contribution was estimated from the standard error of the estimate in the linear fitting (0.5%), which has been included to ensure a conservative uncertainty estimation of $u(V_0^c)$. As a result, a value of 0.7% has been used for $u(V_0^c)$ ($k = 1$). This uncertainty is similar to the value of 0.5% ($k = 1$) found by Toledano et al. (2018) for a single Langley-plot at daytime at Izaña using 15 years of sun photometric measurements. Other authors have studied the impact of additional sources of uncertainty on $u(V_0^c)$, like the effect of the finite bandwidth of the sun photometer spectral bands (Thomason et al., 1982), uncertainty in the air mass determination (Thomason et al., 1983; Forgan, 1988; Russell et al., 1993), systematic diurnal variation in AOD (Marenco, 2007), or systematic semidiurnal cycles in atmospheric pressure or components (Toledano et al., 2018). These contributions are expected to be low or negligible, as stated by Reagan et al. (1986) and Toledano et al. (2018).

We have estimated a total uncertainty ($k = 1$), which can be termed combined standard AOD uncertainty, at $m = 1$ of 0.9–1.0% (1.4% for 440 nm) for Cimel and 0.9% (1.2% for 500 nm) for LunarPFR. The expanded uncertainty (assuming a coverage factor $k = 2$ and therefore a level of confidence of approximately 95%) for these two lunar photometers is 2% (2.8% for 440 nm) and 1.8% (2.4% for 500 nm), respectively.

According to WMO/GAW Report (2005), the uncertainty analysis based on different instruments and measurement methods should include a minimum common denominator principle in order to ensure traceable comparisons. In this work we have adopted the estimation performed by WMO (WMO/GAW Report, 2005) for finite FOV transmission measurements (0.005) for this extra contribution to the u(AOD). Therefore, the total (maximum for $m = 1$) expanded ($k = 2$) AOD uncertainty is expected to range between 0.025 and 0.033 for Cimel, and between 0.023 and 0.029 for LunarPFR.

3.1.2. Lunar-Langley calibration method

This method was specifically designed to account for the change in lunar illumination during the course of the night, as was described in Barreto et al. (2013, 2016). This technique is able to lessen the difficulties in calibrating at night-time because, as in daytime, it only requires one night to calculate the instrument's calibration. This calibration constant should be applied to other lunar cycles and Moon's illumination conditions. The disadvantage of this technique is that it depends on a lunar irradiance model. Barreto et al. (2013, 2016) introduced the contribution of two terms to V_0 in the classic Langley-plot description given in Eq. (1):

$$V_{0,j} = I_{0,j} \cdot \kappa_j \tag{8}$$

where $I_{0,j}$ is the lunar extraterrestrial irradiance in the j^{th} spectral band given by a lunar irradiance model, varying continuously over the Moon's cycle, and κ_j is a constant that depends on the instrument's features. With these two terms, Eq. (1) can be written as follows:

$$ln\left(\frac{V_j}{I_{0,j}}\right) = ln(\kappa_j) - m(\theta)\cdot\tau_j \tag{9}$$

Some previous works (Barreto et al., 2016, 2017; Juryšek and Prouza, 2017) have found that the Cimel AOD uncertainty has a dependence on the lunar phase angle when this calibration technique is applied, with instrumental problems or systematic errors in the lunar irradiance model as the most probable causes for these problems.

We have used this Lunar-Langley technique to calibrate the six Cimel and the LunarPFR photometers. The night of 11–12 June was the common period to obtain the instruments' calibration constants (κ_j) for each and every one of the lunar instruments. This night was confirmed to be clean and stable in terms of aerosol content by means of ancillary information (MPL-3 backscatter profiles), and is characterized by an average phase angle of 27.9° (Moon's illumination of ~ 94%).

Following Barreto et al. (2013, 2016), once the calibration constants κ_j are known, we can determine the AOD from each individual measurement by means of the following expression:

$$AOD_j = \frac{ln(\kappa_j) - ln\left(\frac{V_j}{I_{0,j}}\right) - m_{atm}(\theta)\cdot\tau_{atm,j}}{m_a(\theta)} \tag{10}$$

m_{atm}, m_a, θ and $\tau_{atm,j}$ have been previously described in Eq. (2).

A preliminary uncertainty analysis of the AOD retrieved by a Lunar-Langley calibrated instrument was performed by Barreto et al. (2016). These authors neglected the covariance term between κ and I_0, assuming this term to be low and negative. By doing so, only uncertainties related to instrumental errors were expected to be g-dependent. This assumption seems to be correct provided the lunar irradiance model is not affected by a phase angle dependence in its calibration. However, as Viticchié et al. (2013) observed, a g-dependence of the ROLO calibration does exist. Consequently, the AOD uncertainty in the lunar Langley technique should be revised. In Eq. (11) we present the combined standard uncertainty related to the random uncertainties in the calibration process as a result of the statistical dispersion estimation ($u(\kappa)$), in addition to the systematic uncertainties due to ROLO estimations ($u(I_0)$), in a relative scale as in the previous calibration technique, and the instrument uncertainty ($u(V)$). This combined standard uncertainty, as in the previous calibration technique, is also modulated by the air mass term.

$$u_{AOD^2} = \frac{1}{m^2}\left(\frac{u^2(\kappa)}{\kappa^2} + \frac{u^2(I_0)}{I_0^2} + \frac{u^2(V)}{V^2}\right) + \frac{2}{m^2}\cdot r_{\kappa,I_0}\cdot\left(\frac{\delta AOD}{\delta\kappa}\right)\cdot\left(\frac{\delta AOD}{\delta I_0}\right) \cdot u(\kappa)\cdot u(I_0) \tag{11}$$

In this equation r_{κ,I_0} represents the correlation coefficient between κ and I_0, and $\frac{\delta AOD}{\delta I_0}$ and $\frac{\delta AOD}{\kappa}$ are the partial derivatives of AOD with I_0 and κ, respectively. Similar values as in the previous calibration technique have been assumed for $u(V)$ and $u(\kappa)$ (the same as $u(V_0^c)$). Following Kieffer and Stone (2005), the estimated Type A uncertainty of the ROLO model ($u(I_0)$) can be considered ≤ 1%. In this work, we have estimated the uncertainty component due to the covariance associated to κ and I_0

(last term in Eq. (11)) by means of root mean square (RMS) values of κ versus g-fitted residuals calculated by Juryšek and Prouza (2017).

With all this information, we have a combined standard AOD uncertainty ($k = 1$) for Cimel (at $m = 1$) ranging from 0.015 to 0.017 (to 0.022 in 440 nm) in the case of $g > 45°$, and 0.014 for $g < 45°$ (0.015 for 440 nm). In the case of the LunarPFR, this combined standard uncertainty ($k = 1$) is 0.014–0.018 for $g > 45°$ and 0.012–0.015 for $g < 45°$.

Maximum (at $m = 1$) expanded AOD uncertainty ($k = 2$) is 0.049 for Cimel and 0.041 for LunarPFR.

3.1.3. Sun-Moon Gain Factor method

This third calibration method for lunar photometry was presented in Barreto et al. (2016), based on previous works carried out by Berkoff et al. (2011) and Barreto et al. (2013). This method implies the direct transference of daytime calibration to night-time by means of an estimation of the different amplification (G) used between these two direct sun and moon measurements. Once G is known, it is possible to estimate κ_λ using the following equation:

$$\kappa_\lambda = \frac{E_{0,\lambda}}{V_{0,\lambda} \cdot G} \tag{12}$$

In this equation, $V_{0,\lambda}^{\text{sun}}$ represents the daytime calibration for each channel and $E_{0,\lambda}$ is the extraterrestrial solar irradiance (Gueymard, 2003). A nominal G value of 4096 (given by the manufacturer) has been used in this paper.

Considering that Cimel is the only instrument with capabilities to perform both day and night-time measurements with the same device, this technique can only be applied to Cimel photometers. As Barreto et al. (2016) stated, this Sun-Moon Gain Factor method is not dependent on the lunar irradiance model and therefore, in contrast to the other two techniques, uncertainties in this model are transferred directly to the AOD calculation.

$$u_{\text{AOD}^2} = \frac{1}{m^2}\left(\frac{u^2(V_0^{\text{sun}})}{(V_0^{\text{sun}})^2} + \frac{u^2(G)}{G^2} + \frac{u^2(E_0)}{E_0^2} + \frac{u^2(I_0)}{I_0^2} + \frac{u^2(V)}{V^2}\right) \tag{13}$$

In this case, the uncertainty involved in the lunar irradiance model ($u(I_0)$) is expected to be 5–10% (Kieffer and Stone, 2005). The uncertainty involved in the rest of the terms were calculated by Barreto et al. (2016) (0.5% for the extraterrestrial solar irradiance, 0.2–0.5% for V_0^{sun} in the case of a reference instrument that is Langley-calibrated and 1.1% for G). These values lead to a maximum combined standard ($k = 1$) AOD uncertainty of 10.1% (at $m = 1$), with expected AOD departures of up to 0.101.

The maximum (at $m = 1$) total expanded AOD uncertainty ($k = 2$) is 0.207.

3.1.4. Nocturnal cloud screening for Cimel and LunarPFR

We have ensured a minimum impact of cloud contamination on lunar photometers data by applying a cloud screening algorithm to the master Cimel CE#971, the reference instrument in the AOD comparison. We have used a stability criterion based on Cimel triplets which establishes an empirical threshold in the normalized range between these three consecutive measurements (NR_{triplet} computed as the difference between maximum and minimum, divided by the average value of the triplets). This criterion is imposed on all the instruments' spectral bands (from 1640 nm to 440 nm). We have empirically set this threshold at 0.5% by using data accumulated over a 3-year period at the Izaña Observatory. Taking into account that the triplet stability depends on the incident flux, which in turn, depends on the lunar phase angle, as was observed by Juryšek and Prouza (2017), this empirical threshold should vary throughout the Moon's cycle. Hence, using part of the methodology proposed by Juryšek and Prouza (2017), we propose a cloud screening method based on raw data, in which if the $NR_{triplet}$ exceeds the value of $0.005 \cdot P(g)$ this observation must be rejected due to presumed cloud contamination. $P(g)$ is a function of the Moon's phase given by Juryšek and Prouza (2017).

By performing the cloud screening based on CE#971 data, results for the other lunar photometers involved in the comparison campaign are ensured to be cloud-cleared.

3.2. Stellar photometry calibration and data quality control

The EXCALIBUR star photometer was calibrated using the Astronomical Langley Technique (Perez-Ramirez et al., 2011). Calibration of this instrument is usually performed twice a year at Calar Alto Astronomical Center (37.2°N, 2.5°W, 2368 m a.s.l.). Measurements taken during this field campaign under pristine conditions were used to validate the stability in the EXCALIBUR calibration and relative differences with respect to previous calibrations of less than 1% were found.

Computation of AOD follows the procedure presented in Pérez-Ramárez et al. (2008a, b, 2011). The method of observation in this campaign is the one star method (OSM) (Leiterer et al., 1995; Pérez-Ramárez et al., 2008b; Baibakov et al., 2015) using two stars (Mirfak and Regulus). Stellar photometry is very sensitive to atmospheric turbulence, what is the so-called "seeing-effect" due to natural fluctuations of the atmospheric refractive index (scintillation). For the stellar photometer used here, Pérez-Ramárez et al. (2011) pointed out the low signal-to-noise ratio and the low exposure times for very low AOD (typically below 0.5 s for the wavelengths near the maximum quantum efficiency of the CCD camera) as the causes that produce uncertainties in the measurements because of atmospheric turbulence. Dark current effects on the measurements are appropriately accounted for (Pérez-Ramárez et al., 2008b).

The expected uncertainty in AOD measurements performed by means of stellar photometry has been estimated in 0.02–0.03 by Baibakov et al. (2015) and Pérez-Ramárez et al. (2015). For large AODs (typically above 0.2) the effects of fluctuations are minimized, which allows a better monitoring of day-to-night AODs evolution (Pérez-Ramárez et al., 2012b). However, for very low AODs and measurement times, fluctuations in the signal are frequently observed. Pérez-Ramárez et al. (2011) estimated the AOD error in relatively low AOD conditions at Granada city to be 0.02 for wavelengths below 800 nm and 0.01 for wavelengths above 800 nm.

The EXCALIBUR star photometer follows a specific criterion for cloud-screening and quality control. This procedure involves calculating AOD moving averages and detecting outliers. Final data is averaged every 15 min to smooth fluctuations. Details of the cloud screening and data quality algorithm are described in Pérez-Ramárez et al. (2012b). Note that because CCD camera takes approximately 20 s in reading the image for a particular measurement, the methods based on triplets, such as those performed by the Cimel instruments, are not practicable for cloud screening in the EXCALIBUR star photometer.

3.3. USGS/ROLO

ROLO model is a USGS- and NASA-funded effort to provide accurate exo-atmospheric lunar spectral irradiance estimation for on-orbit calibration of remote sensing satellite instruments (Kieffer and Stone, 2005). This model is based on thousands of Moon images (acquired over more than eight years) from the two ROLO telescopes located in Flagstaff, Arizona, in 32 wavelength bands, from 350 nm to 2450 nm, at phase angles ranging within ± 90°. The ROLO model outputs have an estimated accuracy of 1% in the Moon's reflectance and an expected accuracy in the Moon's irradiance ranging from 5% to 10% (Stone and Kieffer, 2004).

USGS/ROLO lunar extraterrestrial irradiances (I_0) values during the field campaign (June and July) have been provided by the USGS.

4. Results

4.1. ROLO implementation for Moon photometry observation (RIMO)

The RIMO model has been developed by a team formed by members of several institutions: IARC, University of Valladolid (Spain), University of Granada (Spain), ISAC (Italy) and the Czech Academy of Sciences (Czech Republic). The motivation for establishing this consortium is to provide the scientific community with an accessible irradiance model for the near real-time AOD calculations required for aerosol monitoring. For RIMO's development we have used the same empirical formulation in terms of lunar-disk equivalent reflectance presented in Kieffer and Stone (2005) Eq. (10), but taking into account a misleading description of the different variables (T. Stone, personal communication in the 3rd Lunar Workshop, Izaña, 2017). Since this misleading description of variables does not affect the USGS/ROLO outputs, RIMO reflectances are expected to be essentially identical to those provided by the USGS. The revised equation used in our implementation is Eq. (14), and only intends to clarify the terms involved in this lunar reflectance model.

$$ln(A_j) = \sum_{n=0}^{3} a_{i,j} g^i + \sum_{n=1}^{3} b_{n,j} \varphi^{2n-1} + c_1 \cdot \phi + c_2 \cdot \theta + c_3 \cdot \Phi \cdot \phi + c_4 \cdot \Phi \cdot \theta + d_{1,j} \cdot e^{\frac{-g}{p_1}} + d_{2,j} \cdot e^{\frac{-g}{p_2}} + d_{3,j} \cdot cos\left(\frac{g - p_3}{p_4}\right) \quad (14)$$

In this equation, A_j is the lunar disk-equivalent reflectance in the ROLO j^{th} band, g is the absolute phase angle (in radians and degrees), θ and ϕ are the selenographic latitude and longitude of the observer (in degrees), respectively, and Φ is the selenographic longitude of the Sun (in radians). These geometric variables, in addition to the apparent Moon's zenith angle, are calculated by means of the SPICE observation geometry information system (Acton, 1996; Acton et al., 2017), from the NASA's Navigation and Ancillary Information Facility (NAIF). The coefficients of Eq. (14) are the same as in Kieffer and Stone (2005), which helps to calculate the Moon's reflectance in the 32 ROLO wavelengths. A comparison analysis between the different USGS/ROLO and RIMO geometrical inputs in Eq. (14) performed during the field campaign showed rather low relative differences (<±0.1%), with differences of ± 0.06% in the Moon's disk-equivalent reflectances. As a result, the only difference between the two models is expected to come from the subsequent smoothing of the reflectance spectrum.

In this model we have applied the smoothing process described in Kieffer and Stone (2005) to generate $A_{smooth,j}$. The calculated reflectances at the 32 ROLO wavelengths for a specific geometric configuration (g = 7°, Φ= 7° and zero libration) have been normalized by a linear wavelength dependent fit to a composite spectrum of the Moon's soil (95%) and rocks (5%) samples returned from Apollo 16th mission. The ratio between the reflectance A_j from Eq. (14) and the fitted to composite spectrum at the 32 wavelengths obtained for this specific configuration (g = 7°, ϕ = 7° and zero libration) allows us to apply this smoothing process to any other viewing geometry.

Lunar spectral irradiance at the effective wavelength (central wavelength) of each band j (I_j) is calculated by interpolating to the instrument spectral band response both the smoothed disk-equivalent reflectances ($A_{smooth,j}$) and the standard extraterrestrial solar irradiance spectrum (E_j) (Wehrli, 1986) using the following equation:

$$I_j = \frac{A_{smooth,j} \cdot \Omega_M \cdot E_j}{\pi} \quad (15)$$

where Ω_M is the Moon's solid angle ($6.4177 \cdot 10^{-5}$ sr).

Lunar spectral irradiances retrieved using Eq. (15) are corrected from the actual Sun-Moon and viewer-Moon distances using Eq. (7) in Kieffer and Stone (2005).

The new RIMO model is freely available for the scientific community at http://testbed.aemet.es/rimoapp, as a part of the IARC activities of the WMO-CIMO Testbed for Aerosols and Water Vapour Remote Sensing Instruments.

4.2. ROLO and RIMO models evaluation

The differences between the two lunar irradiance models have been evaluated to ensure the suitability of the RIMO model for the AOD calculation. Relative differences (in %) with the Moon's phase angle between the two lunar irradiance models for Izaña site in a 2-month period (June–July, 2017) are shown in Fig. 3 for the six Cimel spectral bands. Low differences (between ± 2%) are observed in the visible spectral bands and in 1020 nm whilst higher differences between −6%

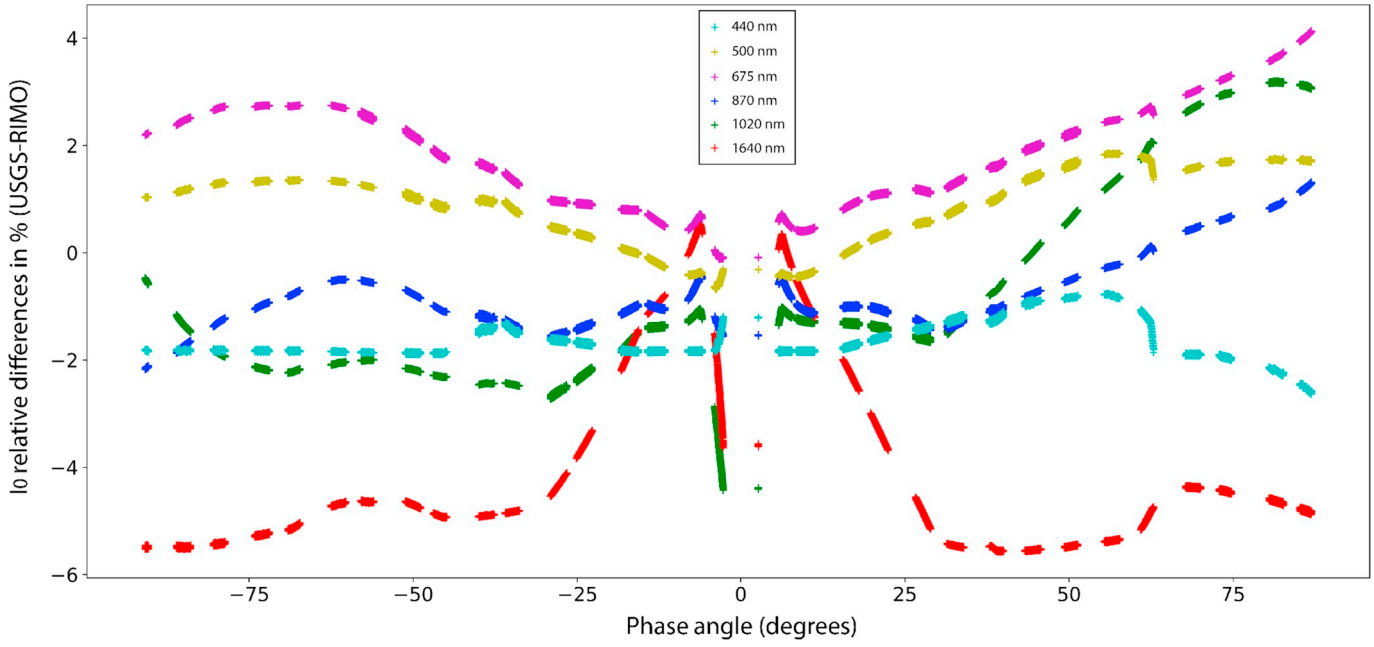

Fig. 3. Relative differences between I_0 from USGS/ROLO and RIMO in June–July 2017 at Izaña for the Cimel wavelengths.

and 1% are observed in 1640 nm. The most noticeable dependence with phase angle is observed in 1640 nm (symmetric about full Moon) and in 1020 nm (asymmetric, with higher values after the full Moon). Relative differences in 870, 675 and 500 nm spectral bands display some dependence with phase angle (higher relative differences of up to 4% from full to last quarter Moon). This dependence on g can be considered negligible in the case of 440 nm (relative differences quite stable around −1% and −2%). The expected difference in AOD (Lunar-Langley calibration applied) as a result of the previous discrepancies between models can be parameterized by the following equation:

$$\Delta(AOD) = \frac{1}{m_a} \cdot ln\left[\frac{I_0^{ROLO} \cdot \kappa_{ROLO}}{I_0^{RIMO} \cdot \kappa_{RIMO}}\right] \quad (16)$$

AOD differences within ± 0.015 are found in this 2-month period when $g < 70°$ for the four coincident spectral bands (440, 500, 675 and 870 nm), while values of up to 0.025 are found for 870 nm and 675 nm when $g > 70°$.

As discussed in Sect 4.1, taking the small relative differences in the inputs/outputs of Eq. (14) into account, the discrepancies in I_j and AOD observed between the two models might be attributed to the different smoothing process applied to the models' outputs.

A coherence day/night/day test analysis using daytime AOD information extracted from AERONET as a reference has been performed in order to check and quantify the night-time AOD difference between the two models. AOD at night-time was calculated using the master Cimel CE#971 data and both the USGS/ROLO and the RIMO irradiance models. This analysis encompasses the day/night AOD comparison performed at the first 1 h of the day and the last 1 h of the night (moonset-sunrise, Fig. 4), and at the last 1 h of the day and the first 1 h of the night (sunset-moonrise, Fig. 5). AOD differences are within ± 0.018, which is the precision limit of radiometric measurements at night for Langley-calibrated instruments (Barreto et al., 2016). This result indicates that the two lunar irradiance models show a quite similar performance during the Moon's cycle.

Once we have compared the two lunar irradiance models and the existence of a significant bias with phase angle in any of them has been discarded, from here on we will use the RIMO model to compute night-time AOD from the different lunar photometers involved in the field campaign.

4.3. Instrumental intercomparison analysis

4.3.1. Raw signals

A raw signal comparison analysis has been carried out by calculating the ratios of coincident spectral signals (dark current corrected) measured by the master Cimel (CE#971) and the five Cimel secondary instruments (Fig. 6). Some outliers were encountered at night-time as a result of an incorrect flagging of the Cimel cloud screening algorithm.

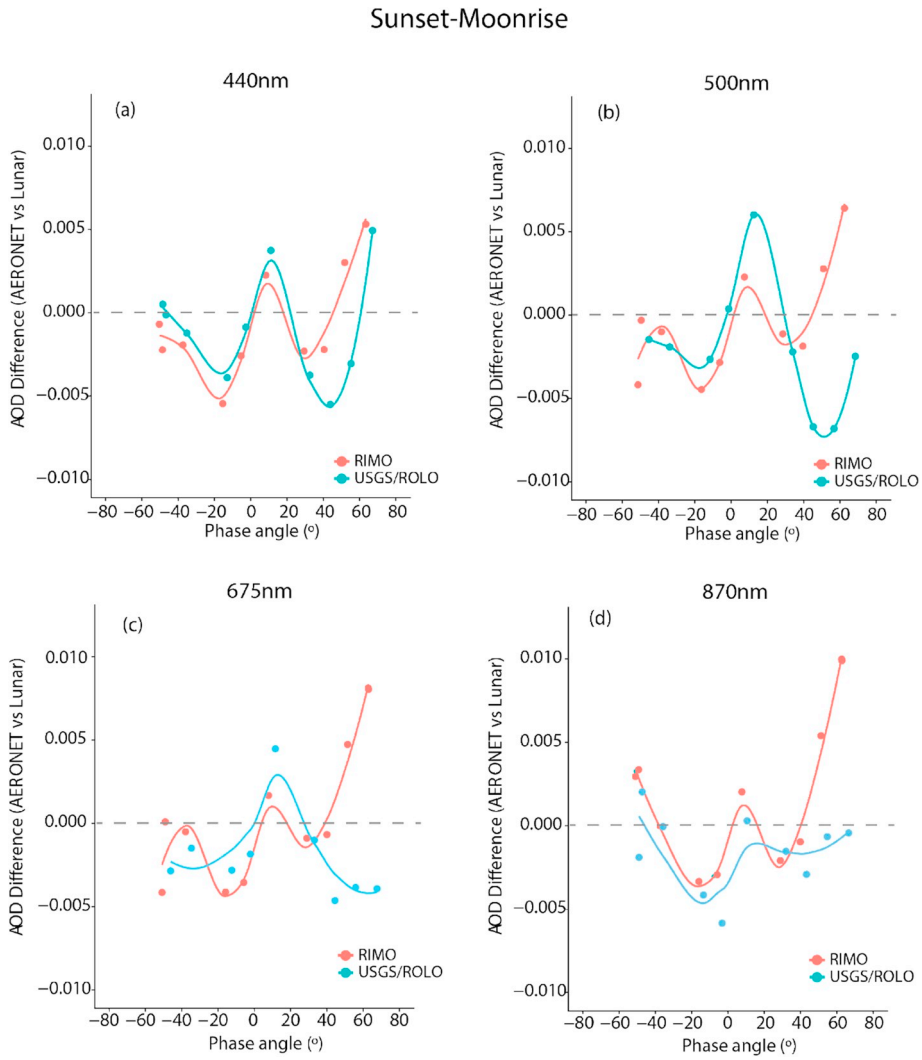

Fig. 4. AOD differences (calculated with RIMO and USGS/ROLO) as a function of phase angle between AERONET daytime and CE#971 night-time data during moonset-sunrise (MS-SR, defined as the last 1 h of nocturnal data vs the first 1 h of daytime data).

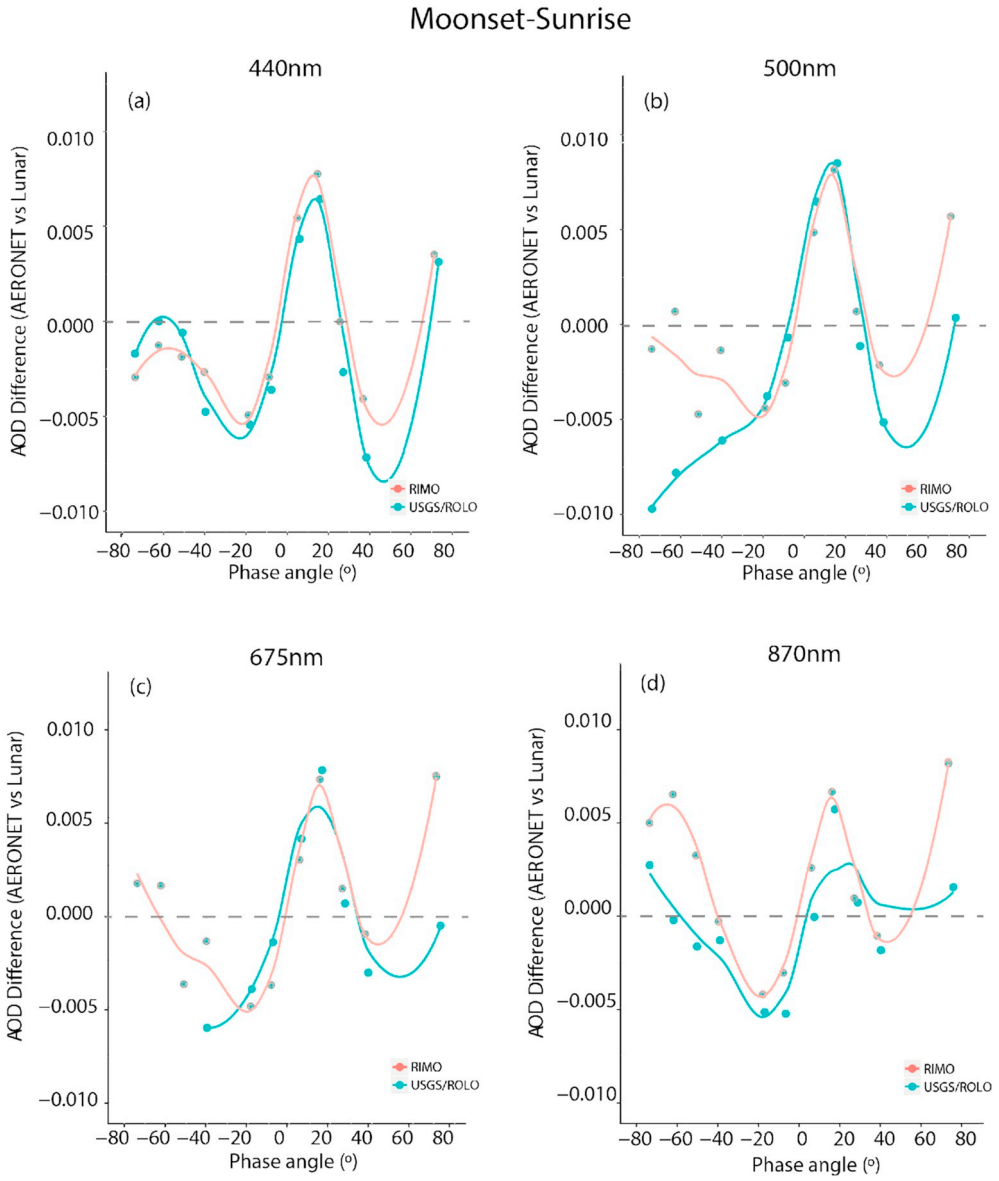

Fig. 5. AOD differences (calculated with RIMO and USGS/ROLO) as a function of phase angle between AERONET daytime and CE#971 night-time data during sunset-moonrise (SS-MR, defined as the last 1 h of daytime data vs the first 1 h of nocturnal data).

These outliers have been subsequently removed to ensure data quality, leading to a data set with 1938, 2223, 1028, 1940 and 1421 pairs for the nocturnal comparison of the CE#971 against the CE#919, CE#915, CE#942, CE#945 and CE#949, respectively. We have a total of 5589, 7348, 8657, 6933 and 5115 pairs for the CE#971 versus CE#919, CE#915, CE#942, CE#945 and CE#949 daytime comparison, respectively. We have considered synchronous measurements in a time window of ± 2 min. The average and standard deviation of ratios have been also quantified in Tables 2 and 3 for day and night-time, respectively. Quite similar day and night ratios are observed in the five different pairs of Cimel instruments. We have obtained relative differences in mean ratios of up to 0.4%, with the exception of 1640 nm spectral band, which showed higher relative differences (up to 1.5%). The higher difference found at 1640 nm is likely to be due to the more sensitive InGaAs sensors installed in the secondary heads. Very low standard deviation (σ) and NR_{ratios} (defined as the difference between maximum and minimum ratios divided by their mean) indicate the stability of Cimel measurements over time. NR_{ratios} higher than 2% were generally found at 440 nm, attributed to the low SNR as a result of the low incoming signal in this spectral range. NR_{ratios} values of 2.27% and 2.87% were also found for the CE#919 at day and night, respectively, in the two spectral bands measured with the InGaAs detector (1020 nm -not shown- and 1640 nm), being attributed to instrumental problems in this sensor head (obstruction found in the instrument's collimator).

Averaged ratios between LunarPFR and cloud-screened CE#971 nocturnal data are shown in Fig. 7. Only the ratios between the three nearly coincident spectral bands have been included in this figure (500, 675 and 870 nm) as well as the linear fit to ratios versus lunar phase angle (solid line in Fig. 7). This figure reveals that ratios in all channels decrease as g increases, more rapidly in the case of 500 nm spectral band. The slope of this linear fitting might be an estimate of the rate of decay, with values of $-4.8{\cdot}10^{-5}$, $-5.8{\cdot}10^{-5}$ and $-2.9{\cdot}10^{-4}$ ($degree^{-1}$) being found for spectral bands centered at 870, 675 and 500 nm, respectively. Looking at Fig. 7, an abrupt change in ratio is evident on three specific nights: 9–10 June (averaged phase angle, $\bar{g}$, of 6.7°), 10–11 June ($\bar{g}$ of 16.7°) and 15–16 June ($\bar{g}$ of 73.9°). This drop observed in the LunarPFR/Cimel ratio, although it is small, might reveal the existence of instrumental differences between the two lunar photometers (e.g. in moon tracking, in the dark current correction or due to in-homogeneities in FOV mostly for the LunarPFR) which might affect

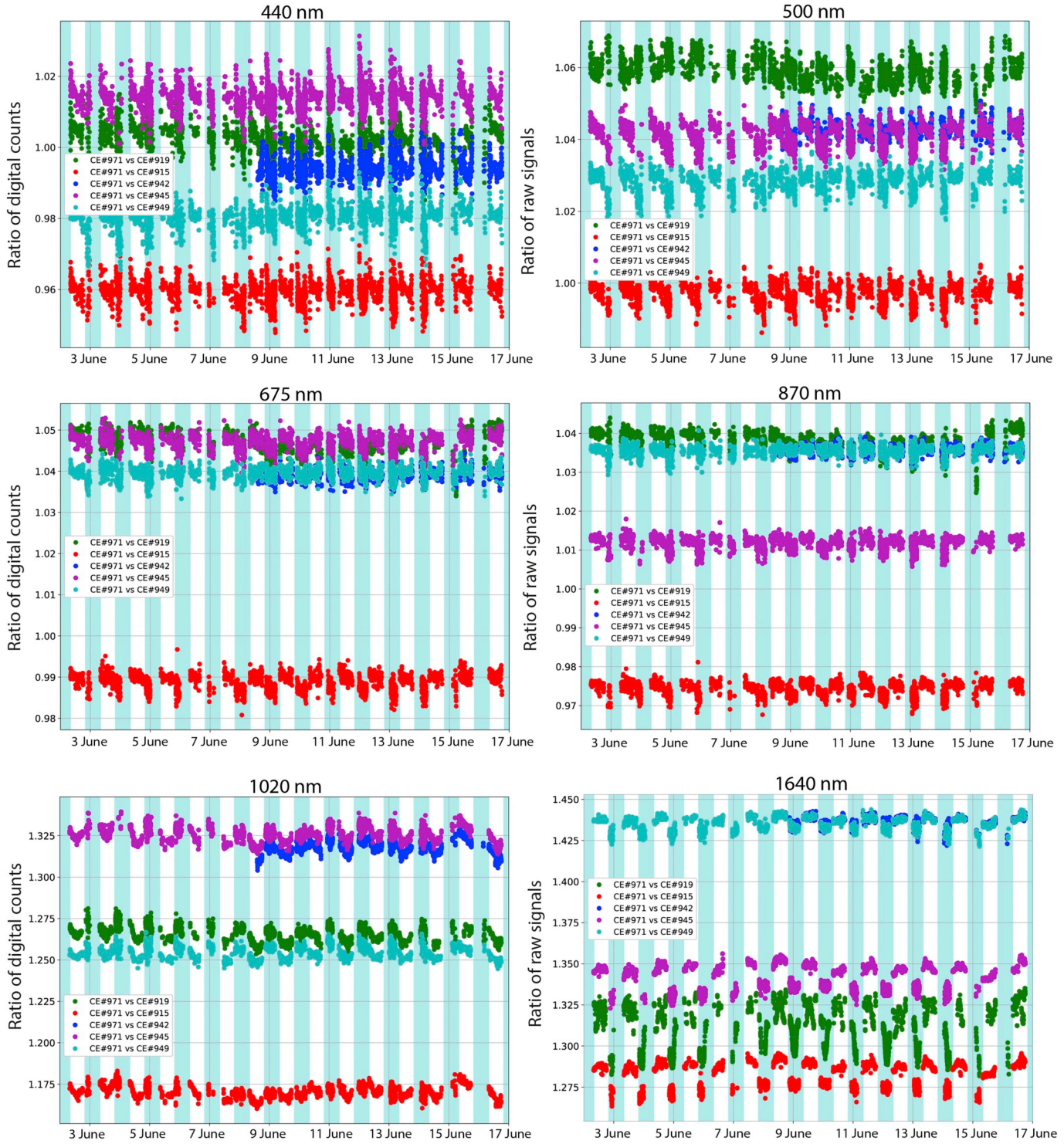

Fig. 6. Ratios of digital counts (dark current corrected) between the master Cimel (CE#971) and the five secondaries for the six different Cimel spectral bands at Izaña, between June 2 and 17, 2017. Night-time data is shaded in blue. (For interpretation of the references to color in this figure legend, the reader is referred to the Web version of this article.)

the derived AOD.

A subsequent raw signal analysis has been performed to enlighten this issue in terms of Cimel, LunarPFR and RIMO calibration constants (V_0^cs). Instruments' calibration constants have been obtained for Cimel and LunarPFR by means of the robust Langley-plot calibration technique (Eq. (4)). We have normalized these V_0^c s to their values when the Moon is full (9 June) to make comparable the calibration constants each night. ROLO V_0^c s were obtained by means of Eq. (8), using the κ_j retrieved by each instrument and the I_{0j}^{ref} in the reference Langley period. The V_0^c evolution for Cimel, LunarPFR and RIMO during the field campaign is shown in Fig. 8 for the three coincident spectral bands (500, 675 and 870 nm). Values close to one correspond to the two nights closer to the full Moon. Monotonically decreasing normalized V_0^c values are found for lower illumination conditions. The differences between the three calibration constants are not readily apparent from this figure. Therefore the relative differences between these normalized

Table 2
Main statistics of daytime raw signals between the master Cimel CE#971 and secondary Cimels: mean, standard deviation (σ), normalized range of ratios (NR_{ratios}) in % and number of coincidences (N).

DAY							
Secondary no.		440 nm	500 nm	675 nm	870 nm	1020 nm	1640 nm
CE#919 (N = 5589)	mean	1.003	1.058	1.048	1.039	1.263	1.322
	σ	0.003	0.003	0.002	0.002	0.004	0.006
	NR_{ratios}	2.21	1.74	1.04	0.87	1.59	2.27
CE#915 (N = 7348)	mean	0.960	0.999	0.990	0.975	1.169	1.288
	σ	0.002	0.001	0.001	0.001	0.004	0.003
	NR_{ratios}	1.86	1.36	1.03	0.90	1.77	1.18
CE#942 (N = 8657)	mean	0.994	1.043	1.039	1.036	1.316	1.436
	σ	0.002	0.002	0.001	0.001	0.004	0.002
	NR_{ratios}	2.02	1.39	0.90	0.63	1.91	0.72
CE#945 (N = 6933)	mean	1.015	1.043	1.048	1.013	1.324	1.347
	σ	0.002	0.002	0.001	0.001	0.004	0.003
	NR_{ratios}	1.85	1.39	0.93	0.99	1.76	1.23
CE#949 (N = 5115)	mean	0.981	1.030	1.040	1.036	1.252	1.438
	σ	0.002	0.001	0.001	0.001	0.002	0.002
	NR_{ratios}	1.87	1.32	0.84	0.73	1.29	0.83

Table 3
Main statistics of night-time raw signals between the master Cimel CE#971 and secondary Cimels: mean, standard deviation (σ), normalized range of ratios (NR_{ratios}) in % and number of coincidences (N).

NIGHT							
Secondary no.		440 nm	500 nm	675 nm	870 nm	1020 nm	1640 nm
CE#919 (N = 1938)	mean	1.001	1.060	1.044	1.036	1.268	1.302
	σ	0.004	0.003	0.002	0.002	0.003	0.009
	NR_{ratios}	3.03	2.00	1.68	0.86	2.06	2.87
CE#915 (N = 2223)	mean	0.958	0.995	0.987	0.972	1.170	1.274
	σ	0.003	0.002	0.001	0.001	0.003	0.003
	NR_{ratios}	2.56	1.68	1.62	1.39	1.92	1.58
CE#942 (N = 1028)	mean	0.993	1.041	1.038	1.035	1.319	1.433
	σ	0.003	0.002	0.001	0.001	0.003	0.002
	NR_{ratios}	2.09	1.35	0.79	0.74	1.17	1.24
CE#945 (N = 1940)	mean	1.013	1.038	1.046	1.011	1.328	1.334
	σ	0.004	0.002	0.001	0.001	0.003	0.003
	NR_{ratios}	3.01	1.63	1.10	0.90	1.67	1.39
CE#949 (N = 1421)	mean	0.978	1.025	1.038	1.035	1.257	1.431
	σ	0.004	0.002	0.001	0.001	0.002	0.003
	NR_{ratios}	2.96	1.59	0.99	1.10	1.54	1.17
LunarPFR (N = 675)	mean	–	0.544	0.310	0.481	–	–
	σ	–	0.007	0.002	0.003	–	–
	NR_{ratios}	–	6.99	4.31	3.58	–	–

V_0^c values are presented in Fig. 9. Consequently, the existence of some differences between these three spectral V_0^c s becomes evident. Cimel is the only instrument with V_0^c information in the whole cycle, showing a systematic overestimation of the Moon's irradiance over the entire cycle with respect to RIMO (up to 3.5%) and in the half cycle with respect to LunarPFR ($\sim$ 3% in 870 nm and 675 nm spectral bands). V_0^c differences are higher as g increases. Lunar irradiance values extracted from LunarPFR are closer to RIMO V_0^c s, within the $\pm$ 1% Type A uncertainty expected for this model.

The systematic lunar irradiance overestimation by Cimel in addition to the decreasing LunarPFR/Cimel ratios indicate that Cimel seems to measure more signal than the LunarPFR as the Moon's irradiance is lower, which could be attributed to the different pointing process of the two lunar photometers. While the LunarPFR points to the center of the Moon, Cimel points to the center of the illuminated part of the Moon, and therefore some differences might exist between the aureole light measured by the two photometers. A possible inaccurate dark current correction performed by Cimel might be also behind the differences observed between Cimel and LunarPFR.

4.3.2. Aerosol optical depth

AOD time series for the two lunar photometers and the stellar photometer at 440, 500, 675 and 870 nm are shown in Figs. 10–13, respectively. In these figures we present two possible ways to retrieve AOD from lunar photometers, depending on the calibration procedure. AOD calculated with the Lunar-Langley calibration (using the RIMO model) is shown in the upper panel whilst AOD calculated by means of the Langley-plot calibration (with the illumination-based correction applied) is shown in the lower panel. Stellar AODs are the same in these two panels. AOD information at daytime has been displayed in yellow, corresponding to AERONET version 3 level 1.5 data measured by the Izaña AERONET master #244 (http://aeronet.gsfc.nasa.gov). Stellar measurements covered the temporal range between 2 June to 9 June, while the LunarPFR measured only from 9 June onwards, due to instrumental problems. CE#971 was the only instrument covering the whole phase angle range. Stellar measurements were averaged every 15 min to reduce noise due to atmospheric turbulence that produces fluctuations in the signals. Despite applying a cloud-screening method to Cimel data, some outliers in AOD can be seen in these figures in 5–7 June, attributed to non-filtered clouds. A wrong cloud flagging is also

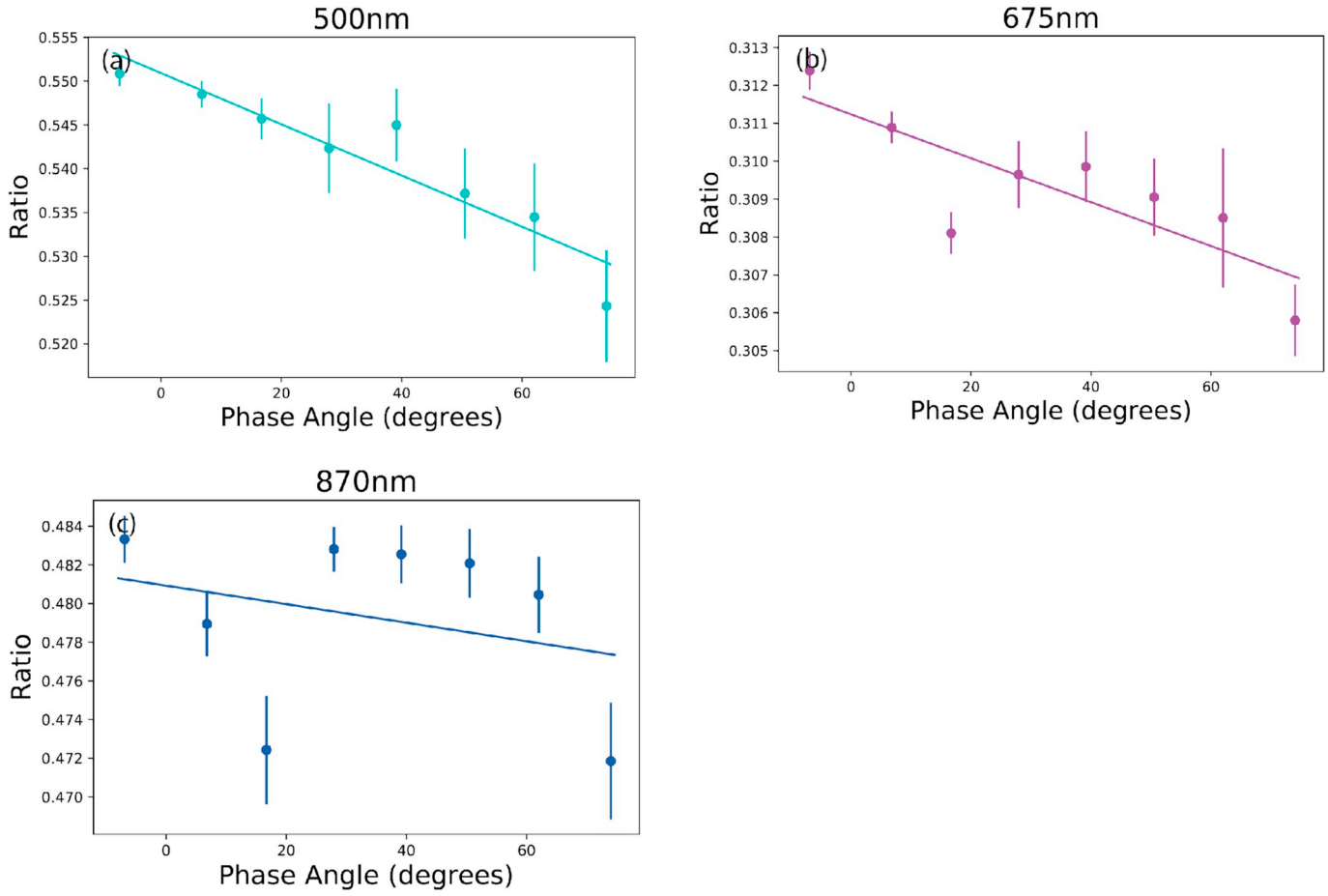

Fig. 7. Ratios of raw signals (night-time only) with the Moon's phase angle (in degrees) between the LunarPFR and the master Cimel (CE#971) for the three near coincident spectral bands: (a) 500, (b) 675 and (c) 870 nm. Solid line represents the x-y linear fitting.

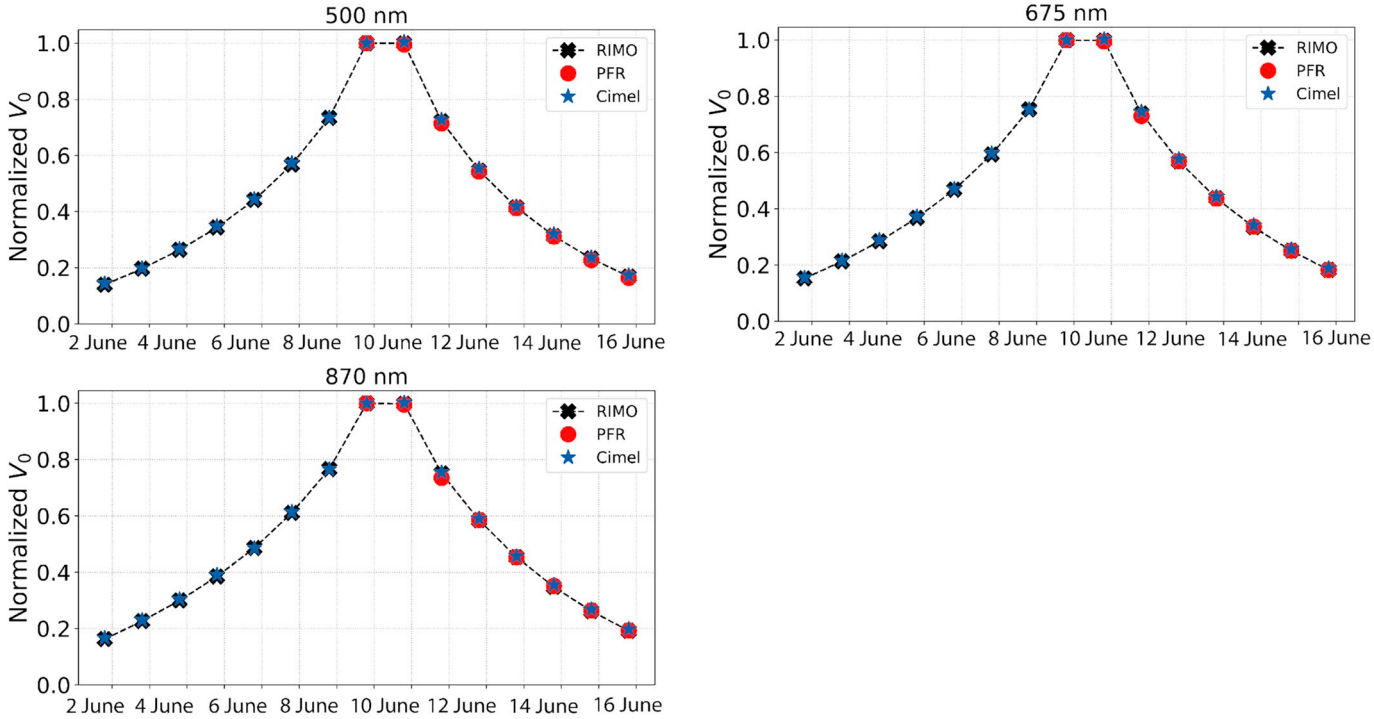

Fig. 8. Evolution during the field campaign of the normalized V_0^c computed from Cimel, LunarPFR and RIMO data, for 500, 675 and 870 nm spectral bands.

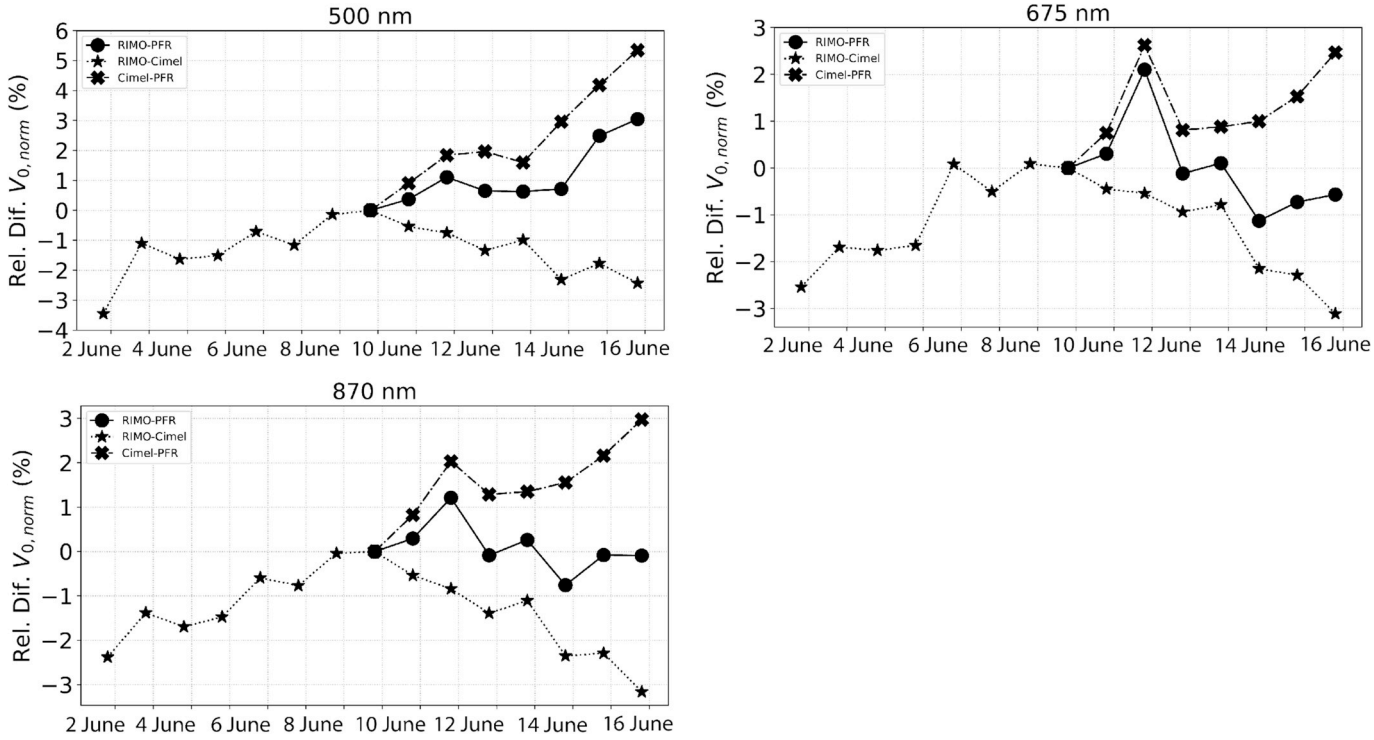

Fig. 9. Relative difference of normalized V_0^c (in %) between Cimel and LunarPFR, as well as between these two instruments and the V_0 computed from the RIMO model, for 500, 675 and 870 nm spectral bands.

observed at daytime.

Despite the 15-min average time applied on stellar photometry data, high AOD dispersion is still observed in the four different spectral bands of the EXCALIBUR star photometer. These fluctuations are mostly associated with the different effects of atmospheric turbulence on each filter. Filters in the visible (e.g. 500 nm and 670 nm) have very low exposure times (<0.5 s) due to the larger quantum efficiency of the CCD camera and the larger emissivity of stars in this spectral region. However, in the UV (e.g. 380 nm) and NIR (e.g. 870 nm) ranges larger exposure times are required (typically larger than 10 s) which minimize

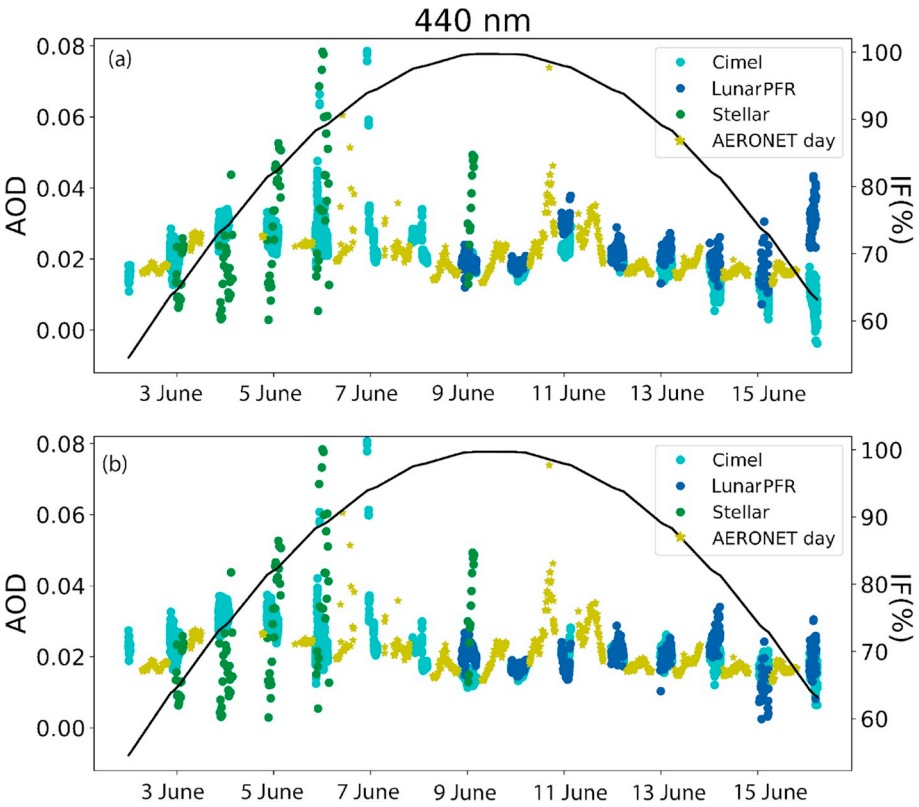

Fig. 10. AOD time series for master Cimel CE#971 (at 439.5 nm), LunarPFR (at 412.4 nm), stellar (at 436.8 nm) and daytime AERONET (at 439.7 nm) in the period 2–17 June 2017. AOD from lunar photometers have been extracted by means of **(a)** Lunar-Langley calibration with the RIMO model, and **(b)** Langley-plot calibration with V_0^c values. The black line and right y axis correspond to the evolution of the Moon's illumination factor (IF, in %) in this period.

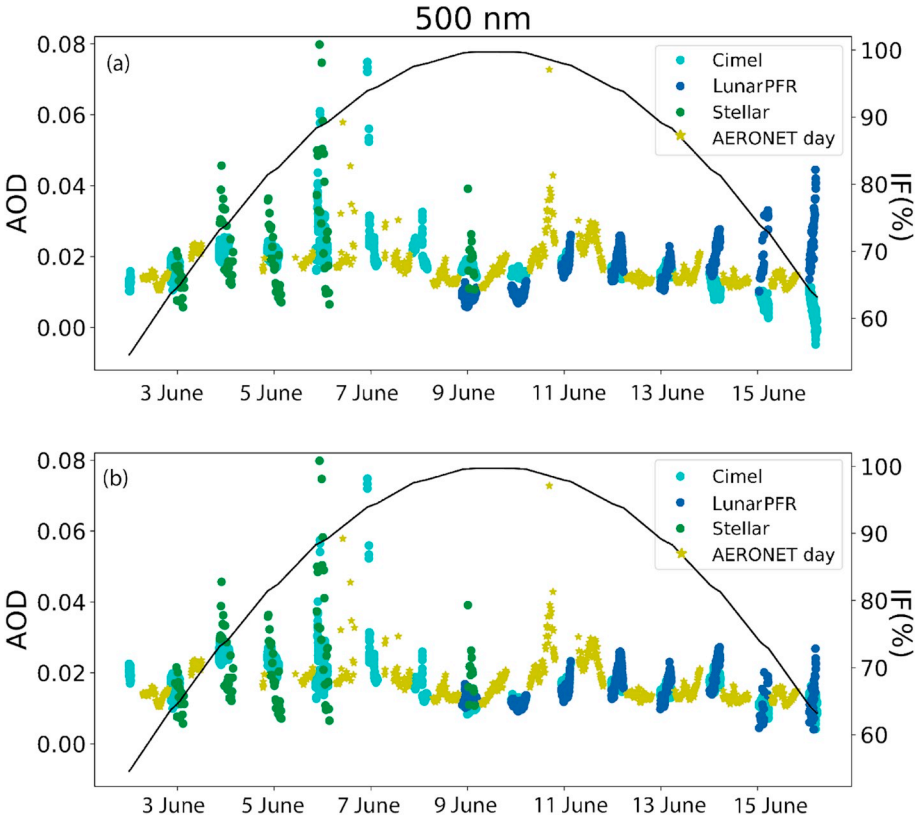

Fig. 11. AOD time series for master Cimel CE#971 (at 500.6 nm), LunarPFR (at 500.7 nm), stellar (at 500.7 nm) and daytime AERONET (at 500.8 nm) in the period 2–17 June 2017. AOD from lunar photometers have been extracted by means of **(a)** Lunar-Langley calibration with the RIMO model, and **(b)** Langley-plot calibration with V_0^c values. The black line and right y axis correspond to the evolution of the Moon's illumination factor (IF, in %) in this period.

the effects of atmospheric turbulence. We note here that CCD camera is cooled at constant −20 °C during all its operation and temperature effects are negligible (Pérez-Ramárez et al., 2008b). These problems imply AOD fluctuations with an amplitude of 0.04, which is near the AOD uncertainty expected for this technique (±0.02–0.03). AOD fluctuations higher than 0.04 were only found at 440 nm spectral band. Cimel AOD dispersion at night-time was found to be lower compared to that observed for star photometry, clearly indicating the higher

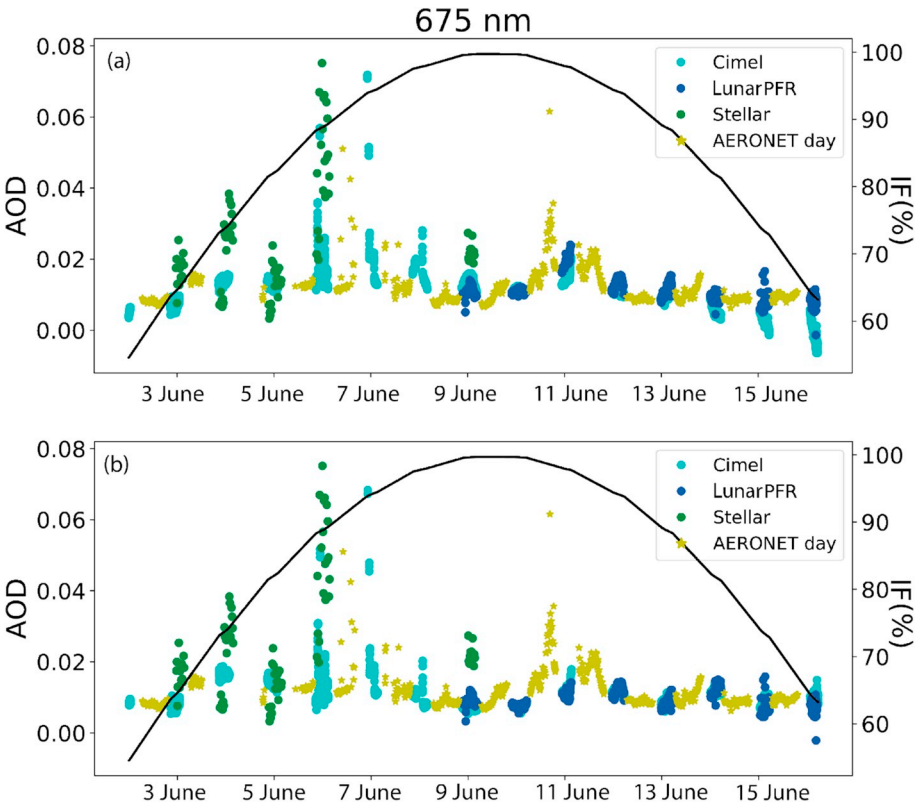

Fig. 12. AOD time series for master Cimel CE#971 (at 674.8 nm), LunarPFR (at 675.6 nm), stellar (at 670.0 nm) and daytime AERONET (at 675.7 nm) in the period 2–17 June 2017. AOD from lunar photometers have been extracted by means of **(a)** Lunar-Langley calibration with the RIMO model, and **(b)** Langley-plot calibration with V_0^c values. The black line and right y axis correspond to the evolution of the Moon's illumination factor (IF, in %) in this period.

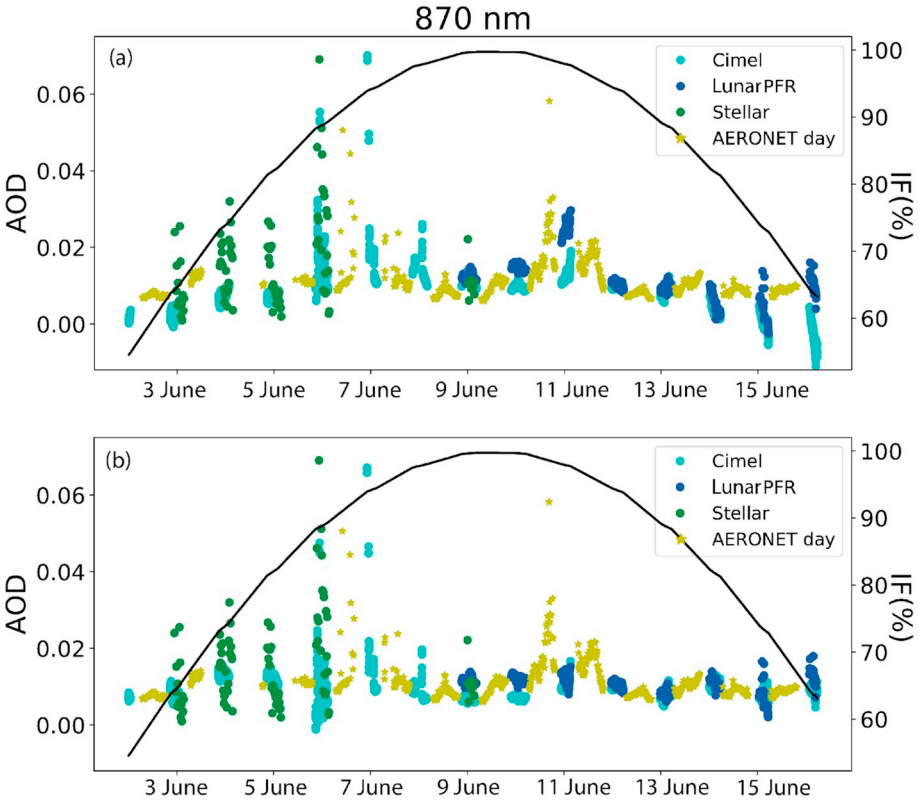

Fig. 13. AOD time series for master Cimel CE#971 (at 870.4 nm), LunarPFR (at 861.3 nm), stellar (at 879.5 nm) and daytime AERONET (at 869.8 nm) in the period 2–17 June 2017. AOD from lunar photometers have been extracted by means of **(a)** Lunar-Langley calibration with the RIMO model, and **(b)** Langley-plot calibration with V_0^c values. The black line and right y axis correspond to the evolution of the Moon's illumination factor (IF, in %) in this period.

sensitivity of moon photometry under very low AOD conditions.

AOD from lunar photometry can be calculated by means of three different calibration techniques. The following is a detailed description of the AOD results using each one.

4.3.2.1. Lunar-Langley calibration. Larger discrepancies between the instruments from 14 June onwards at higher phase angles were found, with unrealistic LunarPFR AOD variations at 500 nm, indicating the presence of some instrumental problems occurring at these illumination conditions that are not yet understood (Fig. 11 (a)).

Another feature to highlight is the presence of a small phase angle dependence in Cimel AODs (Fig. 10 (a) to 13 (a)). We have found decreasing AODs throughout the night with an amplitude higher with the Moon's phase angle, with a lower dependence before the full Moon (when no LunarPFR data is available). This feature results in negative AODs found for g approximately higher than 40° and lower than −40°. The maximum amplitude was found to be low (−0.01 at 870 nm), within the expected uncertainty in AOD measurements. Notwithstanding this dependence seems to be lower in the case of the LunarPFR, a longer AOD data set is needed to provide more conclusive results on that. This AOD pattern for low illumination conditions shows a hyperbolic shape dependent on lunar zenith and phase angles, identical to the AOD discrepancies reported in previous studies (Barreto et al., 2013, 2016, 2017; Juryšek and Prouza, 2017). This AOD cycle is thought to be partly due to the uncertainties in the ROLO/RIMO model and/or to the reported instrumental deficiencies previously described for Cimel radiometer, which are not yet fully understood.

Bivariate (joint) kernel density estimates plots of AOD differences between Cimel against LunarPFR and stellar are used in Figs. 14 and 15, respectively, to visualize and quantify the possible phase angle dependence. These figures are displayed at the coincident spectral bands between photometers. Each color tone represents the respective probability mass of the AOD difference and therefore the two figures give an overall picture of the phase angle dependence on AOD differences. The univariate density distribution of each variable on each axis is also included in this figure. A total of 675 and 76 coincident and cloud-free measurements have been included in this comparison analysis, for Cimel/LunarPFR and Cimel/stellar, respectively. In this case, we have considered synchronous measurements in a time window of ± 2 min. Quite small differences are observed in Fig. 14 in the whole cycle (after the full Moon), mostly within ± 0.005. Absolute AOD differences within the expected uncertainty are observed for 870 nm and 675 nm spectral bands, with values up to 0.015 and 0.01, respectively. Higher discrepancies were found for 500 nm, in which some LunarPFR technical problems were detected in the previous raw signal analysis (up to 0.04, noticed as an increase in the univariate density distribution for AOD difference above 0.03).

Fig. 15 shows the same analysis but including AOD information from Cimel and stellar photometer (an independent source of AOD at night-time). In this figure, restricted to the part of the lunar cycle prior to the full Moon due to data availability, we found little dependence with phase angle (between ± 0.02) in 500, 675 and 870 nm spectral bands. The higher differences found at g~ -40° are attributed to non-filtered high clouds on 5–7 June (see Fig. 2). Differences of up to 0.04 were found at higher phase angles in the case of the 440 nm spectral band (up to −0.06 in the case of 5–7 June presumably due to cloud contamination). These results are within the expected combined uncertainty for stellar and lunar photometry. They are also consistent with the results obtained by Barreto et al. (2016) in a four-night Cimel and stellar AOD comparison performed in 2015 at Granada station. This analysis of lunar against stellar photometry is not able to discriminate by itself the existence of instrumental problems in the lunar photometers or in the lunar irradiance model.

4.3.2.2. Langley-plot calibration. AOD differences within the precision limits (below 0.01) are observed for the two lunar photometers when the Langley-plot calibration technique with the illumination-based correction is applied (Figs. 10(b)–13(b)). An excellent agreement with daytime AOD is found. In this case, instrumental problems in LunarPFR are minimized, as well as the small phase angle dependence observed in

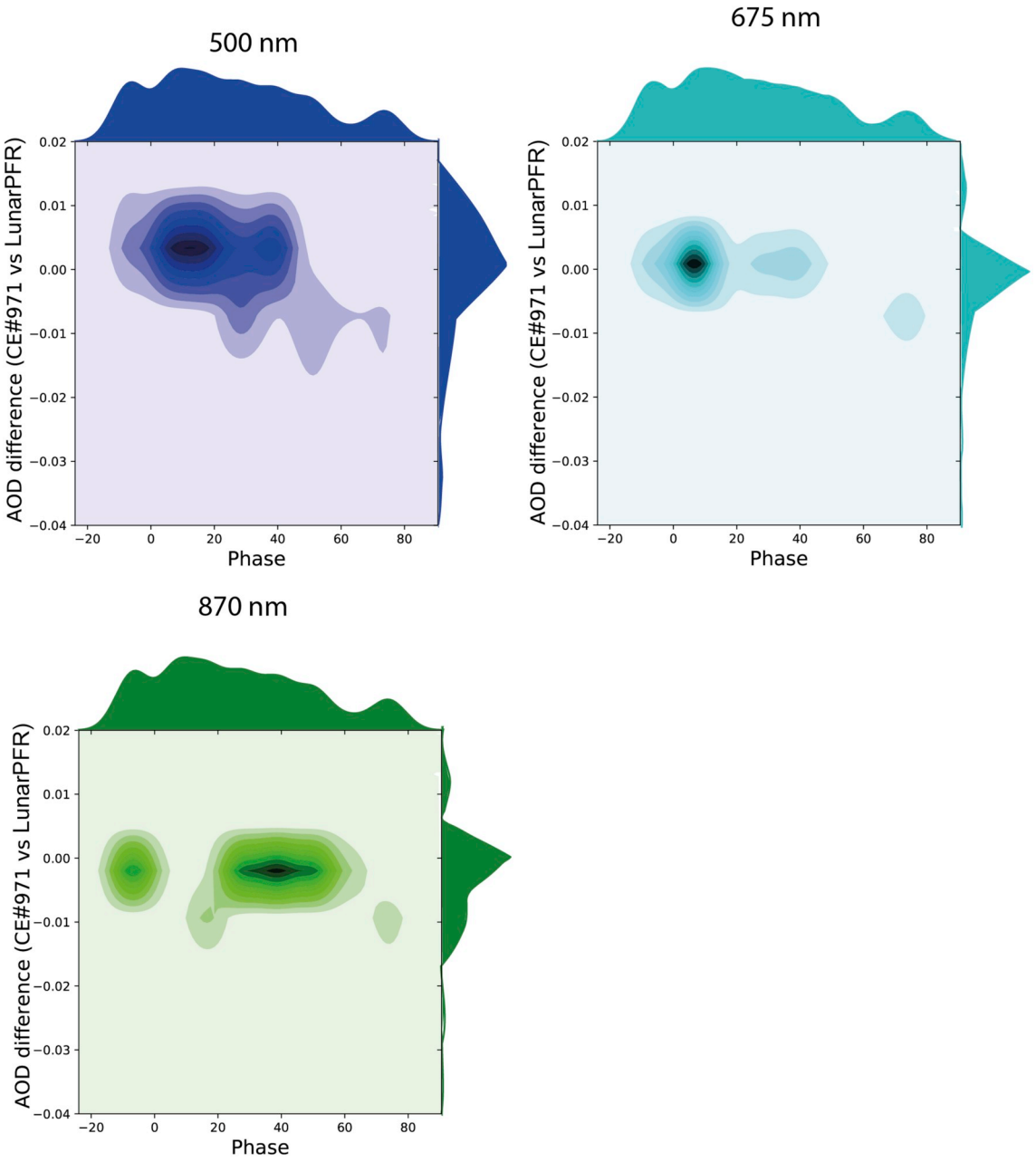

Fig. 14. Bivariate kernel density estimate plots of AOD difference (between CE#971 and LunarPFR) and the Moon's phase angle, calculated with RIMO, for the three coincident spectral bands. Univariate density distribution of each variable is displayed on separate axes.

Cimel AODs, confirming the robustness of this technique.

4.3.2.3. Sun-Moon Gain Factor calibration. The analysis of the AOD retrieved by means of the Sun-Moon Gain Factor technique is displayed in Fig. 16, showing visibly wrong AODs, with strongly negative values (up to -0.09 at $m = 1$) for 500, 675 and 870 nm bands, and strongly positives ones (up to 0.1 at $m = 1$) in the case of 440 nm. It is worth noting that this calibration method is not dependent on the lunar irradiance model and therefore uncertainties on this model are transferred directly to the AOD calculation. These results are in agreement with the $\pm$ 0.10 uncertainty on AOD estimated in Sect. 3.1.3, confirming the uncertainty estimated for the lunar irradiance model (5–10%).

5. Summary and conclusions

In this paper, we present the main results obtained from the first multi-instrument nocturnal intercomparison campaign held in the high-mountain Izaña Observatory during June, 2017. Thus far, this campaign is the first opportunity to compare raw signals and AOD measurements at night from different instruments, such as commercial instruments (six Cimel CE318-T sun-lunar-sky photometers), and non-commercial instruments (a LunarPFR from the World Radiation Center and a stellar photometer from the University of Granada). The main aims of this multi-instrument campaign were: to identify standard procedures to monitor aerosols at night-time; to identify and correct instrumental problems; and finally to offer a lunar irradiance model (ROLO Implementation for Moon photometry Observation, RIMO) freely available to the scientific community (http://testbed.aemet.es/

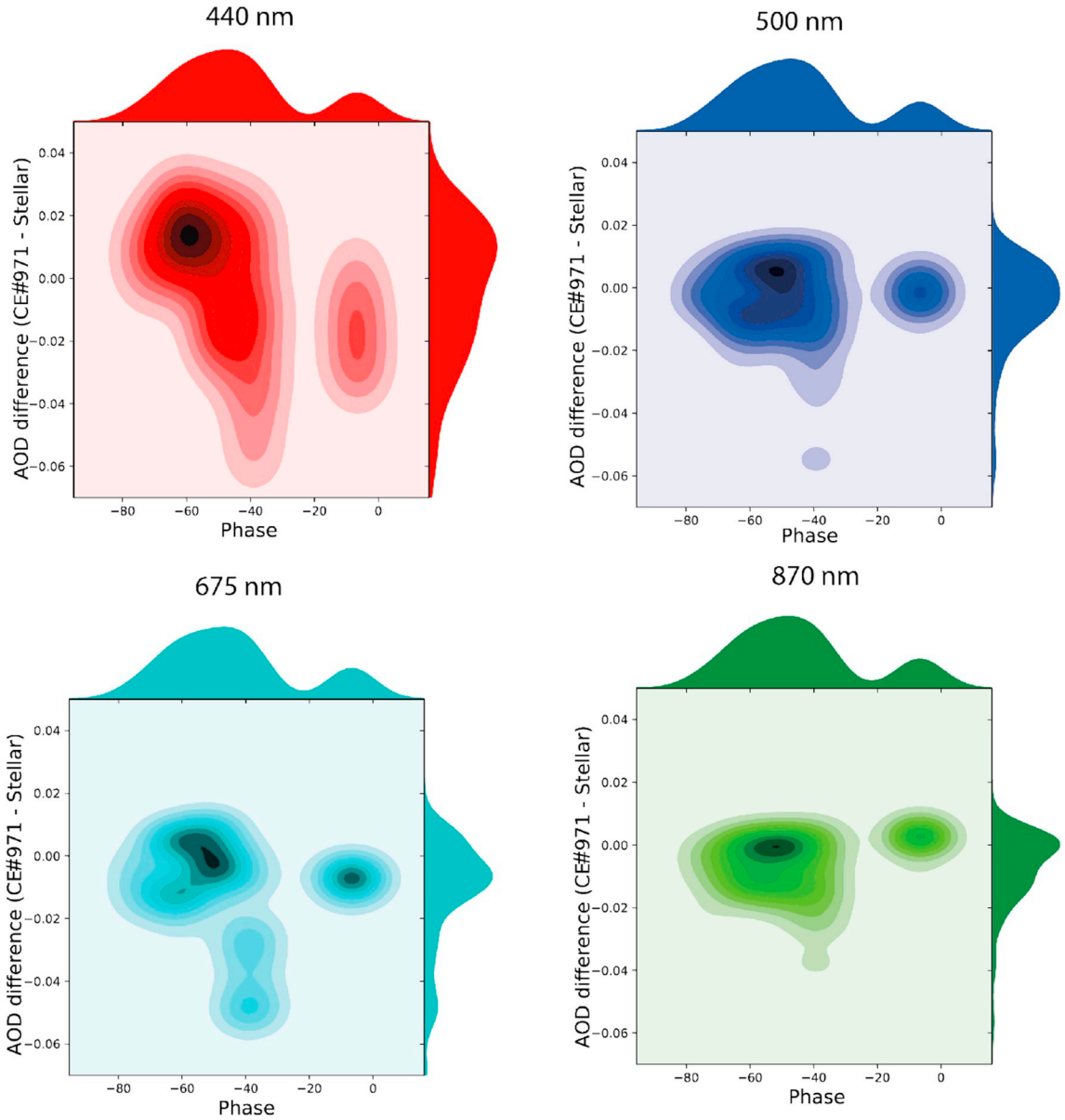

Fig. 15. Bivariate kernel density estimate plots of AOD difference (between CE#971 and stellar) and the Moon's phase angle, calculated with RIMO, for the four coincident spectral bands. Univariate density distribution of each variable is displayed on separate axes.

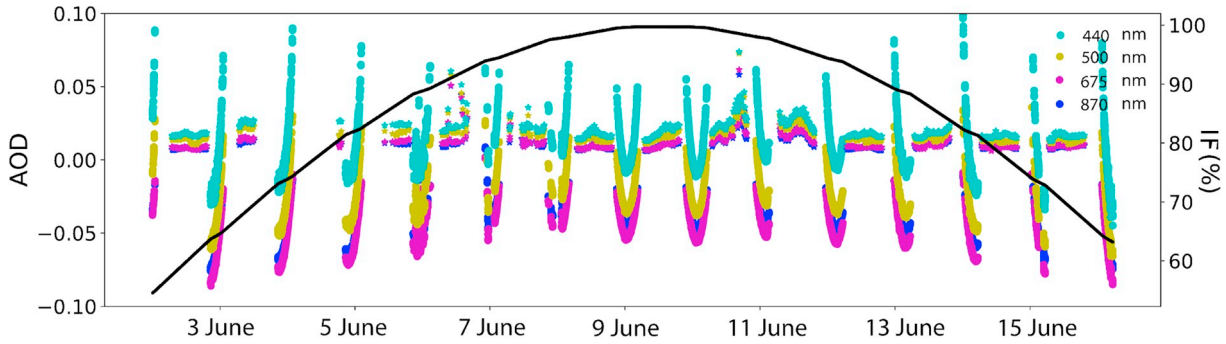

Fig. 16. Nocturnal AOD time series for master Cimel CE#971 (displayed with circles) in the period 2–17 June 2017, for four spectral bands (870, 675, 500 and 440 nm). AODs have been extracted by means of the Sun-Moon Gain Factor calibration. Daytime AODs from AERONET are also displayed with asterisks. The black line and right y axis correspond to the evolution of the Moon's illumination factor (IF, in %) in this period.

rimoapp) until a new, improved lunar irradiance model can be implemented.

In addition to these objectives, we briefly review the different calibration techniques in lunar photometry as well as investigate the existence of possible instrumental differences between the various lunar photometers. These differences might be responsible for the AOD discrepancies previously reported in the literature (Barreto et al., 2016, 2017; Juryšek and Prouza, 2017). The uncertainty estimation of the nocturnal AOD is also an important outcome of the paper.

The main conclusions are:

1. Rather small differences were observed between the AOD calculated using the two lunar irradiance models. We conclude that both models (RIMO and USGS/ROLO) show similar performances during the Moon's cycle and therefore exo-atmospheric lunar irradiances provided can be considered, to a large extent, as equivalent. However, more detailed comparisons between ROLO and RIMO, using reliable and independent observations, are needed to confirm the low reported differences.
2. The comparison analysis in terms of raw signals demonstrates the stability in Cimel's measurements and the existence of a small drop in the LunarPFR/Cimel ratio as the Moon's illumination decreases. This last result points to the existence of some instrumental differences between the two lunar photometers. The analysis of lunar irradiances retrieved using RIMO, Cimel and LunarPFR revealed a slight systematic overestimation of the lunar irradiance by Cimel. Lunar irradiances between these two lunar photometers differ by ~ 3%, which could be attributed to the different pointing processes and pointing uncertainties of the two instruments and/or to a possibly inaccurate dark current correction performed by Cimel. These instrumental differences are not yet fully understood, and longer intercomparison campaigns are needed to better understand them.
3. A relative agreement within ± 3.5% between the RIMO model and the photometer-based lunar irradiances has also been found.
4. The AOD comparison of the two lunar photometers (Cimel and LunarPFR) calibrated by means of the Lunar-Langley calibration method and the RIMO model (with an expected combined AOD standard uncertainty of 0.012–0.022) revealed maximum absolute AOD differences for higher phase angles of up to 0.015 for 870 nm spectral band and 0.01 for 675 nm. Higher differences were found for 500 nm, being attributed to some technical problems in this spectral band. The phase angle dependence on AOD for low illumination conditions found in this work, identical to the AOD discrepancies reported in previous studies, is thought to be partly due to the uncertainties in the RIMO model and to the observed instrumental differences between the two lunar photometers. This small phase angle dependence results in slightly negative AODs (up to −0.01) found for g approximately higher than 40° and lower than −40°, only detected under pristine sky conditions.
5. The AOD analysis performed by means of the robust Langley-plot calibration allowed us to quantify the combined AOD standard uncertainty associated to this calibration technique (up to 0.014). However, the stringent atmospheric conditions required every night to perform this type of calibration makes its routine application to any instrument within a global and operational network impossible.
6. The analysis of the AOD calculated by means of the Sun-Moon Gain Factor technique confirmed the expected uncertainty with AOD for this technique (±0.10) as well as the uncertainty estimated for the lunar irradiance model (5–10%).
7. A subsequent AOD comparative analysis was performed including the AOD retrieved from Cimel and stellar photometers at nominal wavelengths of 440, 500, 675 and 870 nm. In this analysis the stellar photometer can be considered to be an independent source of AOD at night, since its outputs do not depend on any lunar irradiance models. Differences within the expected AOD uncertainty for both photometric techniques (±0.02) were found alongside noticeable AOD fluctuations in star photometry. These fluctuations are associated with the effect of atmospheric turbulence, especially important for low AOD values. Fluctuations in moon photometry have been found to be considerably lower, therefore demonstrating the better capabilities of lunar photometry to measure low aerosol contents.
8. The overall conclusion is that the three types of photometers seem to behave similarly, within their uncertainty limits, and the small AOD differences observed are only detectable in a clean and stable environment such as the Izaña Observatory. Due to the short period of coincident measurements found, some of the conclusions should be confirmed in longer field campaigns.

Declaration of interests

None.

Acknowledgements

This work has been developed within the framework of the activities of the World Meteorological Organization (WMO) Commission for Instruments and Methods of Observations (CIMO) Izaña Testbed for Aerosols and Water Vapour Remote Sensing Instruments. AERONET sun photometers at Izaña have been calibrated within the AERONET Europe TNA, supported by the European Union's Horizon 2020 research and innovation program under grant agreement no. 654109 (ACTRIS–2). CE318-T linearity check has been performed as part of the ESA-funded project "Lunar spectral irradiance measurement and modelling for absolute calibration of EO optical sensors" under ESA contract number: 4000121576/17/NL/AF/hh. LunarPFR has been performing measurements since 2014 in Norway thanks to Svalbard Science Forum funded project, 2014–2016. The authors would like to thank AERONET team for their support and also to NASA's Navigation and Ancillary Information Facility (NAIF) at the Jet Propulsion Laboratory to help the implementation of the "SPICE" ancillary information system used in this study. We also thank Izaña's ITs for their work to implement the RIMO model in the free-access server. Special thanks should be given to Tom Stone, who has kindly provided us with the USGS/ROLO irradiance values used in the model comparison analysis. This work has also received funding from the European Union's Horizon 2020 research and innovation programme and from Marie Skłodowska-Curie Individual Fellowships (IF) ACE-GFAT (grant agreement no. 659398). The authors are grateful to Spanish MINECO (CTM2015-66742-R) and Junta de Castilla y León (VA100P17).

Appendix A. Supplementary data

Supplementary data to this article can be found online at https://doi.org/10.1016/j.atmosenv.2019.01.006.

References

Acton, C.H., 1996. Ancillary data services of NASA's navigation and ancillary information facility. Planet. Space Sci. 44 (No. 1), 65–70.

Acton, C.H., Bachman, N., Semenov, B., Wright, E., 2017. A look toward the future in the handling of space science mission geometry. Planet. Space Sci. https://doi.org/10.1016/j.pss.2017.02.013.

Baibakov, K., O'Neill, N.T., Ivanescu, L., Duck, T.J., Perro, C., Herber, A., Schulz, K.-H., Schrems, O., 2015. Synchronous polar winter starphotometry and lidar measurements at a High Arctic station. Atmos. Meas. Tech. 8, 3789–3809. https://doi.org/10.5194/amt-8-3789-2015.

Barreto, Á., Cuevas, E., Damiri, B., Guirado, C., Berkoff, T., Berjón, A.J., Hernández, Y., Almansa, F., Gil, M., 2013. A new method for nocturnal aerosol measurements with a lunar photometer prototype. Atmos. Meas. Tech. 6, 585–598. https://doi.org/10.5194/amt-6-585-2013.

Barreto, Á., Cuevas, E., Granados-Muñoz, M.-J., Alados-Arboledas, L., Romero, P.M., Gröbner, J., Kouremeti, N., Almansa, A.F., Stone, T., Toledano, C., Román, R., Sorokin, M., Holben, B., Canini, M., Yela, M., 2016. The new Sun-sky-lunar Cimel CE318-T multiband photometer – a comprehensive performance evaluation. Atmos. Meas. Tech. 9, 631–654. https://doi.org/10.5194/amt-9-631-2016.

Barreto, Á., Román, R., Cuevas, E., Berjón, A.J., Almansa, A.F., Toledano, C., González, R., Hernández, Y., Blarel, L., Goloub, P., Guirado, C., Yela, M., 2017. Assessment of nocturnal aerosol optical depth from lunar photometry at the Izaña high mountain observatory. Atmos. Meas. Tech. 10, 3007–3019. https://doi.org/10.5194/amt-10-3007-2017.

Benavent-Oltra, J.A., Román, R., Granados-Muñoz, M.J., Pérez-Ramírez, D., Ortiz-Amezcua, P., Denjean, C., Lopatin, A., Lyamani, H., Torres, B., Guerrero-Rascado, J.L., Fuertes, D., Dubovik, O., Chaikovsky, A., Olmo, F.J., Mallet, M., Alados-Arboledas, L., 2017. Comparative assessment of GRASP algorithm for a dust event over Granada (Spain) during ChArMEx-ADRIMED 2013 campaign. Atmos. Meas. Tech. 10, 4439–4457. https://doi.org/10.5194/amt-10-4439-2017.

Berkoff, T.A., Sorokin, M., Stone, T., Eck, T.F., Hoff, R., Welton, E., Holben, B., 2011. Nocturnal aerosol optical depth measurements with a small-aperture automated photometer using the moon as a light source. J. Atmos. Ocean. Technol. 1. https://doi.org/10.1175/JTECH-D-10-05036.

Campbell, J.R., Hlavka, D.L., Welton, E.J., Flynn, C.J., Turner, D.D., Spinhirne, J.D., Scott, V.S., Hwang, I.H., 2002. Full-time, eye-safe cloud and aerosol lidar observation at atmospheric radiation measurement program sites: instrument and data processing. J. Atmos. Ocean. Technol. 19, 431–442. https://doi.org/10.1175/1520-0426(2002)019¡0431:FTESCA¿2.0.CO;2.

Chaikovsky, A., Dubovik, O., Holben, B., Bril, A., Goloub, P., Tanré, D., Pappalardo, G., Wandinger, U., Chaikovskaya, L., Denisov, S., Grudo, J., Lopatin, A., Karol, Y., Lapyonok, T., Amiridis, V., Ansmann, A., Apituley, A., Alados-Arboledas, L., Binietoglou, I., Boselli, A., D'Amico, G., Freudenthaler, V., Giles, D., Granados-Muñoz, M.J., Kokkalis, P., Nicolae, D., Oshchepkov, S., Papayannis, A., Perrone, M.R., Pietruczuk, A., Rocadenbosch, F., Sicard, M., Slutsker, I., Talianu, C., De Tomasi, F., Tsekeri, A., Wagner, J., Wang, X., 2016. Lidar-Radiometer Inversion Code (LIRIC) for the retrieval of vertical aerosol properties from combined lidar/radiometer data: development and distribution in EARLINET. Atmos. Meas. Tech. 9, 1181–1205. https://doi.org/10.5194/amt-9-1181-2016.

Cesnulyte, V., Lindfors, A.V., Pitkänen, M.R.A., Lehtinen, K.E.J., Morcrette, J.-J., Arola, A., 2014. Comparing ECMWF AOD with AERONET observations at visible and UV wavelengths. Atmos. Chem. Phys. 14, 593–608. https://doi.org/10.5194/acp-14-593-2014.

Cuesta, J., Flamant, H.P., Flamant, C., 2008. Synergetic technique combining elastic backscatter lidar data and sunphotometer AERONET inversion for retrieval by layer of aerosol optical and microphysical properties. Appl. Optic. 47, 4598–4611.

Cuevas, E., Camino, C., Benedetti, A., Basart, S., Terradellas, E., Baldasano, J.M., Morcrette, J.J., Marticorena, B., Goloub, P., Mortier, A., Berjón, A., Hernández, Y., Gil-Ojeda, M., Schulz, M., 2015. The MACC-II 2007–2008 reanalysis: atmospheric dust evaluation and characterization over northern Africa and the Middle East. Atmos. Chem. Phys. 15, 3991–4024. https://doi.org/10.5194/acp-15-3991-2015.

Cuevas, E., Milford, C., Bustos, J.J., del Campo-Hernández, R., García, O.E., García, R.D., Gómez-Peláez, A.J., Guirado-Fuentes, C., Marrero, C., Prats, N., Ramos, R., Redondas, A., Reyes, E., Rodríguez, S., Romero-Campos, P.M., Schneider, M., Belmonte, J., Yela, M., Almansa, F., Barreto, A., López-Solano, C., Basart, S., Terradellas, E., Afonso, S., Bayo, C., Berjón, A., Bethencourt, J., Carreño, V., Castro, N.J., Cruz, A.M., Damas, M., De Ory-Ajamil, F., García, M.I., Gómez-Trueba, V., González, Y., Hernández, C., Hernández, Y., Hernández-Cruz, B., Jover, M., León-Luís, S.F., López-Fernández, R., López-Solano, J., Rodríguez, E., Rodríguez-Franco, J.J., Rodríguez-Valido, M., Sálamo, C., Sanromá, E., Santana, D., Santo Tomás, F., Sepúlveda, E., Sierra, M., Sosa, E., 2017. In: Cuevas, E., Milford, C., Tarasova, O. (Eds.), Izaña Atmospheric Research Center Activity Report 2015-2016. State Meteorological Agency (AEMET), Madrid, Spain and World Meteorological Organization, Geneva, Switzerland, NIPO 014-17-012-9, WMO/GAW Report No. 236.

Cuevas, E., Romero-Campos, P.M., Kouremeti, N., Kazadzis, S., García, R.D., Barreto, A., Guirado-Fuentes, C., Ramos, R., Toledano, C., Almansa, F., Gröbner, J., 2018. Aerosol Optical Depth comparison between GAW-PFR and AERONET-Cimel radiometers from long term (2005–2015) 1-minute synchronous measurements. Atmos. Meas. Tech. Discuss. https://doi.org/10.5194/amt-2018-438.

Dubovik, O., Sinyuk, A., Lapyonok, T., Holben, B.N., Mishchenko, M., Yang, P., Eck, T.F., Volten, H., Muñoz, O., Veihelmann, B., van der Zander, Sorokin, M., Slutsker, I., 2006. Application of light scattering by spheroids for accounting for particle non-sphericity in remote sensing of desert dust. J. Geophys. Res. 111. https://doi.org/10.1029/2005JD006619.

Esposito, F., Serio, C., Pavesse, G., Auriemma, G., Satriano, C., 1998. Measurements of nighttime atmospheric optical depth. Preliminary data from mountain site in southern Italy. J. Aerosol Sci. 29, 1213–1218.

Fernald, F.G., 1984. Analysis of atmospheric lidar observations: some comments. Appl. Opt. 5, 652–653. https://doi.org/10.1364/AO.23.000652.

Forgan, B.W., 1988. Bias in a solar constant determination by the Langley method due to structured atmospheric aerosol: comment. Appl. Opt. 27, 2546–2548. https://doi.org/10.1364/AO.27.002546.

Gueymard, C., 2003. The sun's total and spectral irradiance for solar energy applications and solar radiation models. Sol. Energy 76, 423–453. https://doi.org/10.1016/j.solener.2003.08.039.

Herber, A., Thomason, L.W., Gernandt, H., Leiterer, U., Nagel, D., Schulz, K.-H., Kaptur, J., Albrecht, T., Notholt, J., 2002. Continuous day and night aerosol optical depth observations in the Arctic between 1991 and 1999. J. Geophys. Res. Atmos. 107https://doi.org/10.1029/2001JD000536. AAC6.1–AAC6.13.

Holben, B.N., Eck, T.F., Slutsker, I., Tanré, D., Buis, J.P., Setzer, A., Vermote, E., Reagan, J.A., Kaufman, Y.J., Nakajima, T., Lavenu, F., Jankowiak, I., Smirnov, A., 1998. AERONET- A federated instrument network and data archive for aerosol characterization. Rem. Sens. Environ. 66, 1–16.

Jokinen, T., Kontkanen, J., Lehtipalo, K., Manninen, H.E., Aalto, J., Porcar-Castell, A., Garmash, O., Nieminen, T., Ehn, M., Kangasluoma, J., Junninen, H., Levula, J., Duplissy, J., Ahonen, L.R., Rantala, P., Heikkinen, L., Yan, C., Sipilä, M., Worsnop, D.R., Bäck, J., Petäjä, T., Kerminen, V.-M., Kulmala, M., 2017. Solar eclipse demonstrating the importance of photochemistry in new particle formation. Sci. Rep. 7, 45707. https://doi.org/10.1038/srep45707.

Juryšek, J., Prouza, M., 2017. Sun/Moon photometer for the Cherenkov Telescope Array - first results. In: Proceedings of Science, 35th International Cosmic Ray Conference - ICRC2017.

Kieffer, H.H., 1997. Photometric stability of the lunar surface. Icarus 130, 323–327.

Kasten, F., Young, A.T., 1989. Revised optical air mass tables and approximation formula. Appl. Opt. 28, 4735–4738.

Kieffer, H.H., Stone, T.C., 2005. The spectral irradiance of the moon. Astron. J. 129, 2887–2901.

Klett, J.D., 1985. Lidar inversion with variable backscatter/extinction ratios. Appl. Opt. 11 (24), 1638–1643. https://doi.org/10.1364/AO.24.001638.

Kouremeti, N., Gröbner, J., Kazadzis, S., Pfiffner, D., Soder, R., 2016. Development of a Lunar PFR. pp. 21. https://www.pmodwrc.ch/wp-content/uploads/2017/09/2015_Annual_Report.pdf.

Lacherade, S., Viticchié, B., Stone, T., Lebégue, L., Wagner, S., Hewison, T., 2013. On the phase-angle dependence of the moon calibration results. GSICS Quat.: Lunar Calib. 7 (3).

Lacherade, S., Aznay, O., Fougnie, B., Lebégue, L., 2014. POLO: a unique dataset to derive the phase angle dependence of the Moon irradiance. In: Proc. SPIE 9241, Sensors, Systems, and Next-Generation Satellites XVIII, https://doi.org/10.1117/12.2067283. 924112 (October 7, 2014).

Leiterer, U., Naebert, A., Naebert, T., Alekseeva, G., 1995. A new star photometer developed for spectral aerosol optical thickness measurements in Lindenberg. Contrib. Atmos. Phys. 68, 133–141.

Li, J., Li, X., Carlson, B.E., Kahn, R.A., Lacis, A.A., Dubovik, O., Nakajima, T., 2016. Reducing multisensor satellite monthly mean aerosol optical depth uncertainty: 1. Objective assessment of current AERONET locations. J. Geophys. Res. Atmos. 121https://doi.org/10.1002/2016JD025469. 13,609-13,627.

Lopatin, A., Dubovik, O., Chaikovsky, A., Goloub, P., Lapyonok, T., Tanré, D., Litvinov, P., 2013. Enhancement of aerosol characterization using synergy of lidar and sun-photometer coincident observations: the GARRLiC algorithm. Atmos. Meas. Tech. 6, 2065–2088. https://doi.org/10.5194/amt-6-2065-2013.

Marenco, F., 2007. On Langley plots in the presence of a systematic diurnal aerosol cycle centered at noon: A comment on recently proposed methodologies. J. Geophys. Res. Atmos. 112, D06205. https://doi.org/10.1029/2006JD007248.

Mazzola, M., Stone, R.S., Herber, A., Tomasi, C., Lupi, A., Vitale, V., Lanconelli, C., Toledano, C., Cachorro, V.E., O'Neill, N.T., Shiobara, M., Aaltonen, V., Stebel, K., Zielinski, T., Petelski, T., Ortiz de Galisteo, J.P., Torres, B., Berjón, A., Goloub, P., Li, Z., Blarel, L., Abboud, I., Cuevas, E., Stock, M., Schulz, K.-H., Virkkula, A., 2012. Evaluation of sun photometer capabilities for retrievals of aerosol optical depth at high latitudes: the POLAR-AOD intercomparison campaigns. Atmos. Environ. 52, 4–17. https://doi.org/10.1016/j.atmosenv.2011.07.042.

McArthur, L.J.B., Halliwell, D.H., Niebergall, O.J., O'Neill, N.T., Slusser, J.R., Wehrli, C., 2003. Field comparison of network sun photometers. J. Geophys. Res. 108 (D19), 4596.

Nakajima, T., Tonna, G., Rao, R., Boi, P., Kaufman, Y., Holben, B.N., 1996. Use of sky, brightness measurements from ground for remote sensing of particulate polydispersions. Appl. Opt. 35, 2672–2686.

O'Neill, N.T., Baibakov, K., Hesaraki, S., Ivanescu, L., Martin, R.V., Perro, C., Chaubey, J.P., Herber, A., Duck, T.J., 2016. Temporal and spectral cloud screening of polar winter aerosol optical depth (AOD): impact of homogeneous and inhomogeneous clouds and crystal layers on climatological-scale AODs. Atmos. Chem. Phys. 16, 12753–12765. https://doi.org/10.5194/acp-16-12753-2016.

Pérez-Ramírez, D., Aceituno, J., Ruiz, B., Olmo, F.J., Alados-Arboledas, L., 2008a. Development and calibration of a star-photometer to measure the aerosol optical depth: Smoke observations at a high mountain site. Atmos. Environ. 42, 2733–2738.

Perez-Ramírez, D., Ruiz, B., Aceituno, J., Olmo, F.J., Alados–Arboledas, L., 2008b. Application of Sun/star photometry to derive the aerosol optical depth. Int. J. Rem. Sens. 29 (17–18), 5113–5132.

Pérez-Ramírez, D., Lyamani, H., Olmo, F.J., Alados Arboledas, L., 2011. Improvements in star photometry for aerosol characterizations. J. Aerosol Sci. 4, 737–745.

Pérez-Ramírez, D., Lyamani, H., Olmo, F.J., Whiteman, D.N., Navas-Guzmán, F., Alados-Arboledas, L., 2012a. Cloud screening and quality control algorithm for star photometer data: assessment with lidar measurements and with all-sky images. Atmos. Meas. Tech. 5, 1585–1599. https://doi.org/10.5194/amt-5-1585-2012.

Pérez-Ramírez, D., Lyamani, H., Olmo, F.J., Whiteman, D.N., Alados-Arboledas, L., 2012b. Columnar aerosol properties from sun-and-star photometry: statistical comparisons and day-to-night dynamic. Atmos. Chem. Phys. 12, 9719–9738.

Pérez-Ramírez, D., Veselovskii, I., Whiteman, D.N., Suvorina, A., Korenskiy, M., Kolgotin, A., Holben, B., Dubovik, O., Siniuk, A., Alados-Arboledas, L., 2015. High temporal resolution estimates of columnar aerosol microphysical parameters from spectrum of aerosol optical depth by linear estimation: application to long-term AERONET and star-photometry measurements. Atmos. Meas. Tech. 8, 3117–3133. https://doi.org/10.5194/amt-8-3117-2015.

Reagan, J.A., Thomason, L.W., Herman, B.M., Palmer, J.M., 1986. Assessment of atmospheric limitations on the determination of the solar spectral constant from ground-based spectroradiometer measurements. IEEE T. Geosci. Remote GE-24, 258–266. https://doi.org/10.1109/TGRS.1986.289645.

Román, R., Torres, B., Fuertes, D., Cachorro, V.E., Dubovik, O., Toledano, C., Cazorla, A., Barreto, A., Bosch, J.L., Lapyonok, T., González, R., Goloub, P., Perrone, M.R., Olmo, F.J., de Frutos, A., Alados-Arboledas, L., 2017. Remote sensing of lunar aureole with a sky camera: Adding information in the nocturnal retrieval of aerosol properties with GRASP code. Rem. Sens. Environ. 196, 238–252. https://doi.org/10.1016/j.rse.2017.

05.013.
Russell, P.B., Livingston, J.M., Pueschel, R.F., Reagan, J.A., Browell, E.V., Toon, G.C., Newman, P.A., Schoeberl, M.R., Lait, L.R., Pfister, L., Gao, Q., Herman, B.M., 1993. Post-Pinatubo optical depth spectra vs. latitude and vortex structure: Airborne tracking sunphotometer measurements in AASE II. Geophys. Res. Lett. 20, 2571–2574. https://doi.org/10.1029/93GL03006.
Sayer, A.M., Hsu, N.C., Bettenhausen, C., Jeong, M.-J., 2013. Validation and uncertainty estimates for MODIS Collection 6 "Deep Blue" aerosol data. J. Geophys. Res. Atmos. 118, 7864–7872. https://doi.org/10.1002/jgrd.50600.
Shaw, G.E., 1979. Aerosols at Mauna Loa: optical properties. J. Atmos. Sci. 36, 862–869. https://doi.org/10.1175/1520-0469(1979)036¡0862:AAMLOP¿2.0.CO;2.
Shaw, G.E., 1983. Sun photometry. Bull. Am. Meteorol. Soc. 64, 4–10. https://doi.org/10.1175/1520-0477(1983)064¡0004:SP¿2.0.CO;2.
Spinhirne, J.D., Rall, J.A.R., Scott, V.S., 1995. Compact eye safe lidar systems. Rev. Laser Eng. 23, 112–118.
Stone, T.C., Kieffer, H.H., 2004. Assessment of uncertainty in ROLO lunar irradiance for on-orbit calibration. In: Proc. SPIE 5542, Earth Observing Systems IX, https://doi.org/10.1117/12.560236. (26 October 2004). https://doi.org/10.1117/12.560236.
Stone, R.S., Herber, A., Vitale, V., Mazzola, M., Lupi, A., Schnell, R.C., Dutton, E.G., Liu, P.S.K., Li, S.-M., Dethloff, K., Lampert, A., Ritter, C., Stock, M., Neuber, R., Maturilli, M., 2010. A three-dimensional characterization of Arctic aerosols from airborne Sun photometer observations: PAM-ARCMIP, April 2009. J. Geophys. Res. 115, D13203. https://doi.org/10.1029/2009JD013605.
Tanré, D., Bréon, F.M., Deuzé, J.L., Dubovik, O., Ducos, F., François, P., Goloub, P., Herman, M., Lifermann, A., Waquet, F., 2011. Remote sensing of aerosols by using polarized, directional and spectral measurements within the A-Train: the PARASOL mission. Atmos. Meas. Tech. 4, 1383–1395. https://doi.org/10.5194/amt-4-1383-2011.
Theocharous, E., Ishii, J., Fox, N.P., 2004. Absolute linearity measurements on HgCdTe detectors in the infrared region. Appl. Opt. 43, 4182–4188.
Thomason, L.W., Herman, B.M., Schotland, R.M., Reagan, J.A., 1982. Extraterrestrial solar flux measurement limitations due to a Beer's law assumption and uncertainty in local time. Appl. Opt. 21, 1191–1195. https://doi.org/10.1364/AO.21.001191.
Thomason, L.W., Herman, B.M., Reagan, J.A., 1983. The effect of atmospheric attenuators with structured vertical distributions on air mass determinations and langley plot analyses. J. Atmos. Sci. 40, 1851–1854.
Toledano, C., González, R., Fuertes, D., Cuevas, E., Eck, T.F., Kazadzis, S., Kouremeti, N., Gröbner, J., Goloub, P., Blarel, L., Román, R., Barreto, Á., Berjón, A., Holben, B.N., Cachorro, V.E., 2018. Assessment of Sun photometer Langley calibration at the high-elevation sites Mauna Loa and Izaña. Atmos. Chem. Phys. 18, 14555–14567. https://doi.org/10.5194/acp-18-14555-2018.
Tomasi, C., Vitale, V., Lupi, A., Di Carmine, C., Campanelli, M., Herber, A., Treffeisen, R., Stone, R.S., Andrews, E., Sharma, S., Radionov, V., von Hoyningen-Huene, W., Stebel, K., Hansen, G.H., Myhre, C.L., Wehrli, C., Aaltonen, V., Lihavainen, H., Virkkula, A., Hillamo, R., Ström, J., Toledano, C., Cachorro, V.E., Ortiz, P., de Frutos, A.M., Blindheim, S., Frioud, M., Gausa, M., Zielinski, T., Petelski, T., Yamanouchi, T., 2007. Aerosols in polar regions: A historical overview based on optical depth and in situ observations. J. Geophys. Res. 112, D16205.
Tomasi, C., Lupi, A., Mazzola, M., Stone, R.S., Dutton, E.G., Herber, A., Radionov, V.F., Holben, B.N., Sorokin, M.G., Sakerin, S.M., Terpugova, S.S., Sobolewski, P.S., Lanconelli, C., Petkov, B.H., Busetto, M., Vitale, V., 2012. An update on polar aerosol optical properties using POLAR-AOD and other measurements performed during the International Polar Year. Atmos. Environ. 52 (2012), 29–47. ISSN 1352-2310. https://doi.org/10.1016/j.atmosenv.2012.02.055.
Tomasi, C., Kokhanovsky, A.,A., Lupi, A., Ritter, C., Smirnov, A., O'Neill, N.T., Stone, R.S., Holben, B.N., Nyeki, S., Wehrli, C., Stohl, A., Mazzola, M., Lanconelli, C., Vitale, V., Stebel, K., Aaltonen, V., de Leeuw, G., Rodriguez, E., Herber, A.B., Radionov, V.F., Zielinski, T., Petelski, T., Sakerin, S.M., Kabanov, D.M., Xue, Y., Mei, L., Istomina, L., Wagener, R., McArthur, B., Sobolewski, P.S., Kivi, R., Courcoux, Y., Larouche, P., Broccardo, S., Piketh, S.J., 2015. Aerosol remote sensing in polar regions. Earth Sci. Rev. 140, 108–157. ISSN 0012-8252. https://doi.org/10.1016/j.earscirev.2014.11.001.
Torres, B., Dubovik, O., Fuertes, D., Schuster, G., Cachorro, V.E., Lapyonok, T., Goloub, P., Blarel, L., Barreto, A., Mallet, M., Toledano, C., Tanré, D., 2017. Advanced characterisation of aerosol size properties from measurements of spectral optical depth using the GRASP algorithm. Atmos. Meas. Tech. 10, 3743–3781. https://doi.org/10.5194/amt-10-3743-2017.
Viticchié, B., Wagner, S., Hewison, T., Stone, T., 2013. Lunar calibration of MSG/SEVIRI solar bands. GSICS Quat.: Lunar Calib. 7, 3–5.
Wehrli, C., 1986. Spectral Solar Irradiance Data. WMO ITD 149. WMO, Geneva.
WMO/GAW experts workshop on a global surface-based network for long-term observations of column aerosol optical properties, Report no. 162, Davos, Switzerland, https://library.wmo.int/pmb_ged/wmo-td_1287.pdf, 2005.
Zhang, J., Reid, J.S., 2010. A decadal regional and global trend analysis of the aerosol optical depth using a data-assimilation grade over-water MODIS and Level 2 MISR aerosol products. Atmos. Chem. Phys. 10, 10949–10963. https://doi.org/10.5194/acp-10-10949-2010.